On the Statistical Relationship between Sea Ice Freeboard and C-Band Microwave Backscatter – A^{REV2} : Case Study with Sentinel-1 and Operation IceBridge

Siqi Liu¹, Shiming Xu^{1,2}, Wenkai Guo³, Yanfei Fan¹, Lu Zhou⁴, Jack Landy³, Malin Johansson³, Weixin Zhu¹, and Alek Petty⁵

Correspondence: Shiming Xu (xusm@tsinghua.edu.cn)

Abstract. In this study, we evaluate the statistical relationship between sea ice freeboard and C-band microwave backscatter. By collocating observations between Sentinel-1 images and Operation IceBridge (OIB) measurements in April 2019, we evaluate their relationship under various sea ice types and thickness regimes. We show that, at various spatial scales relevant to synthetic aperture radar (SAR) observations, there exists an apparent significant correlation between C-band backscatter and sea ice freeboard. This relation depends on physical parameters of the sea ice, including the ice type, as well as sensor-specific parameters such as the observational incidence angle of the SAR satellite. As a result, there is considerable variability in this apparent relationship and its fitted parameters. Using the fitted relationship, two-dimensional freeboard maps can be predicted at the scale of SAR images' effective resolution (i.e., ~200^REVI:_m). More importantly, we demonstrate that although the resolution of SAR images are relatively lower than OIB freeboard maps, we can predict the high-resolution, meter-scale freeboard distribution where altimetry measurements are not available. Thus the representation of altimetric measurements can be improved with the upscaling based on the SAR image. The proposed method can be further utilized for the upscaling of satellite based sea ice topography measurements by the Ice, Cloud, and land Elevation Satellite-2 (ICESat-2). Related issues, including the limitation to spring data, scale dependency and the locality of the statistical relationship, as well as the upscaling of current and historical satellite campaigns, are further discussed.

Copyright statement. TEXT

¹Department of Earth System Science, Tsinghua University, Beijing, China

²University Cooperation of Polar Research, Beijing, China

³UiT – The Arctic University of Norway, Tromsø, Norway

⁴Institute for Marine and Atmospheric Research, Department of Physics, Utrecht University, Utrecht, The Netherlands

⁵Earth System Science Interdisciplinary Center (ESSIC) of the University of Maryland, University of Maryland, College Park, MD, USA

1 Introduction

30

Polar sea ice has undergone drastic changes in response to global climate change (Kwok, 2018). As Arctic sea ice coverage diminishes at a substantial rate, there has also been a rapid decrease in ice thickness and volume (Sumata et al., 2023). In particular, sea ice topography, characterized by the small-scale sea ice height variability, has become smoother (Krumpen et al., 2025). Satellite altimetry serves as the backbone for observations of the circumpolar sea ice freeboard and thickness. For both laser and radar altimeters, the signals are sent from the satellites to Earth. By measuring the time difference between the emitted pulse from the satellite and the returned echo, the range between the satellite and the reflecting surface on Earth is estimated. The differentiation of the range of echoes returned from sea ice floes versus interstitial leads gives the radar or laser freeboard, and the sea ice thickness is then calculated from hydrostatic assumptions and the buoyancy relationship. In particular, NASA's ICESat-2 (IS2) satellite is a photon-counting laser altimeter that has carried out continuous observations in both polar regions since 2018 (Markus et al., 2017). Six laser beams of IS2 form into three strong-weak pairs, providing continuous ground coverage in the satellite's flight direction. Validation efforts with airborne campaigns that collocate with IS2 beam segments, including NASA's Operation IceBridge (MacGregor et al., 2021, OIB) and MOSAiC (Nicolaus et al., 2022), show that IS2 is able to achieve highly accurate measurements of the sea ice topography (Kwok et al., 2019; Ricker et al., 2023).

Despite their advantages, satellite altimeters have limited coverage over the sea ice cover. The spatial sampling is inherently confined within the nadir of the satellite's track. For example, the three IS2 beam pairs are within ~3^{REVI:} km of its ground track. In order to attain basin-scale coverage, samples collected throughout the whole month are usually needed. However, within a month's time, the sea ice may have undergone significant changes due to both thermodynamic and dynamic processes. These changes cannot be represented by the aggregated monthly freeboard and thickness maps. Furthermore, the altimetric scans only cover limited area within typical passive microwave imagers' footprints, thus hindering the synergy with these observations (Xu et al., 2017). REV3: For example, L band passive microwave radiometer such as the one onboard the Soil Moisture and Ocean Salinity (SMOS) satellite have complementary observational capabilities to altimeters, and they can be physically synergized for the simultaneous retrieval of sea ice thickness and snow depth (Xu et al., 2017; Zhou et al., 2018; 40 Ricker et al., 2017). However, compared with SMOS's daily basin coverage, much longer periods are needed to obtain an overlapping wide geographic coverage from altimeters such as IS2. Also, small scale features such as sea ice (refrozen) leads greatly modulate the L band brightness temperature (TB, see Zhou et al., 2017), but they are potentially not sampled by line scans of altimeters. For example, previous studies (e.g., Fig. A2 of Zhou et al., 2018) show that a remarkable reduction of the TB uncertainty can be achieved with better coverage of freeboard measurements within the SMOS's footprint.

In this paper we explore the potential of improving the laser altimeter's representation through a synergy with microwave backscatter measurements by synthetic aperture radars (SAR). In particular, the C-band SAR payloads onboard European Space Agency's (ESA's) Sentinel-1 (S1) satellites provide pan-Arctic coverage since 2014 through the Extra-Wide (EW) swath mode scans. In this study, we establish statistical relationships between OIB-based sea ice topographic and freeboard measurements and SAR backscatter normalized radar cross section (σ_0) from S1 scenes using collocated observations during April, 2019. OIB flights during this month, in particular the Airborne Topographic Mapper (ATM) measurements, were intentionally collocated

with IS2 tracks. The ATM measurements feature higher resolution and wider swaths than IS2 measurements, enabling the analysis of co-variability between freeboard and σ₀ at multiple scales. Therefore, they are used to study the upscaling of IS2 measurements. In Section 2 we introduce details of the data used and the processing protocols. Using these statistical relationships, we further design an algorithm prototype for SAR-based prediction and upscaling of laser altimetry (REV2: , as comprehensively described in Section 3. And Section 4 covers the statistical analysis under various sea ice conditions. The locality and limitations of the prediction algorithm are also investigated, along with other related issues in Section 5. (REV2: Finally, Section 5 includes a summary and the outlook to future work.)

2 Data and protocols

2.1 OIB campaigns in April, 2019

During April 2019 four OIB campaigns were carried out in the Arctic (Fig. 1), which were collocated with IS2 and consequently provided validation data for the sea ice elevation (ATL07, see also: Kwok et al., 2019) and freeboard products (ATL10). In particular, the flights on April 8th and 12th were organized **REVI:** into **racetracksin** a **racetrack pattern** and cover more than 200**REVI:** km** along the corresponding IS2 ground tracks, with outbound (i.e., northbound) and inbound (i.e., southbound) flight passes covering beam pair of **#3-#4* and **1-#2*, respectively. Two different types of conic scans of ATM onboard these OIB campaigns were carried out: the 15° wide swath scan that covers about 500**REVI:** m** across the flight pass, and the 2.5° narrow swath scan that covers about **REV3:** 8060**REVI:** m**. The scan angle of the wide-swath scanners is 15°, resulting in a swath width of 500**REVI:** m**. The scan angle of the narrow-swath scanners is 2.5°, which enhances the shot density in the central part of the wide swath. In addition, there are three flight passes of the racetrack, and together they cover over 1**REVI:** km** in the cross-track/flight path direction. Furthermore, the campaign on April 8th dominantly covered areas with thick multi-year ice (MYI), while that on April 12th sampled more interstitial first-year ice (FYI) within the MYI. Two other flights on April 19th and 22nd are longer tracks that traverse both MYI and FYI (Fig. 1). **REV2:**Based on ERA5** data for the study period, the large-scale atmospheric conditions were typical of the late-winter conditions in the respective regions. There were no sudden warming events or significant precipitation that potentially changes the SAR backscatter signature of the sea ice.

In order to fully utilize the ATM measurements on April 8th and 12th, we construct a merged sea ice freeboard map using all three OIB passes. The left and middle passes were about 1.25 hours apart, while the right and middle passes were about 2.5 hours apart. Full details of the processing are covered in Appendix A. Briefly, first, we retrieve the total freeboard (denoted F_s) within the entire ATM swath for each pass, using the raw elevation measurements by ATM. Second, we obtain the $1^{REVI:}$ m-scale F_s map for each pass through spatial linear interpolation. The scan pattern of the ATM results in a variable number of shot spacings within the scan swath, with relatively lower shot density in the middle (Petty et al., 2016). To mitigate uncertainty introduced by this spatial sampling non-uniformity, the irregularly spaced ATM elevation data are converted to a regularly spaced $1^{REVI:}$ m F_s map. Finally, the F_s maps of the three passes are stitched together after collocation, producing the F_s map that covers $\sim 1500^{REVI:}$ m in the cross-flight direction.

PREVIS: The standard OIB Level4 (L4) product includes F_s parameter derived from ATM measurements and geolocated aerial photography. It employs a lead discrimination algorithm, which utilizes geolocated aerial photography to identify local sea surface height, thereby enhancing the quality and number of sea surface height determinations. The final product is gridded to a 40 m along-track resolution and can serve as a validation reference for the newly constructed 1 m-scale F_s maps. REV3: The newly constructed 1m-scale F_s maps are validated with the standard OIB Level4 (L4) product. Specifically, we coarsen the F_s map to match the 40 REV1: m resolution and the location (nadir to the flight) of the L4 product. Validations show strong agreement, with RMSE of 0.15^{REV1} : m on April 8th and 0.1^{REV1} : m on April 12th at 40^{REV1} : m scale. At 400^{REV1} : m scale, RMSE further decreased to 0.04^{REV1} : m on April 8th and 0.03^{REV1} : m on April 12th (Fig. S1). Hence the 1^{REV1} : m-scale F_s maps are used further for the statistical analysis with SAR images.

2.2 S1 EW images and sea ice type maps

100

105

110

Both S1A and S1B data are available during the study period of April 2019. EW mode images with dual polarization channels (HH and HV) are accessed and collocated with the aforementioned OIB observations. The SAR incidence angles (IA) across the swath range from 20° to 46° for S1's EW mode. EW mode images use TOPSAR techniques to achieve a very large swath coverage ($\sim 400 \ km$), but TOPSAR acquisitions are affected by the "scalloping effect" (De Zan and Guarnieri, 2006). Additionally, the noise floor varies with range position, creating discontinuous sharp intensity changes known as the "banding effect" (Lohse et al., 2021; Sun and Li, 2021). These issues are particularly prominent in the HV channel due to its low signal-to-noise ratio (SNR) (Segal et al., 2020). Details of the SAR images, including the image identifiers and the acquisition times, are provided in Tab. B1. Each image is preprocessed using ESA's Sentinel Application Platform (SNAP, version 11.0.0). Processing steps include the application of precise orbit files, thermal noise correction, radiometric calibration, and terrain correction. Finally, we convert the backscatter intensities into σ_0 .

REV2: Sea ice type information is derived from S1 images using a classifier specifically accommodating per class IA dependencies of SAR intensities (HIH and HV) and gray-level co-occurrence matrix (GLCM) textures (Lohse et al., 2020; Guo et al., 2023). Details of this classifier are introduced in Appendix B. REV2: Sea ice type information is derived from S1 images and the sea ice classification algorithm used in this study is based on: Lohse et al. (2020) and Guo et al. (2025). Lohse et al. (2020) developed a supervised algorithm that accounts for the class-dependent IA effects, known as the GIA classifier. While this classifier performs well in addressing IA sensitivity, some misclassifications and ambiguities remain. To address these issues, Guo et al. (2025) enhanced the algorithm by incorporating GLCM texture features, resulting in improved class separation. This study uses this classification approach to produce sea ice type maps on the selected S1 scenes.

In the classification process, seven GLCM textures are derived from the HH channel of each SAR image, with a texture window size of 11 pixels. Then, SAR intensities (HH and HV) and GLCM textures (HH) are used as input to the GIA classifier, which incorporates their IA dependencies. Sea ice is classified into three types: level first-year ice (LFYI), deformed first-year ice (DFYI), and multiyear ice (MYI). To further refine the results, a Markov Random Field based contextual smoothing process is applied with a window size of 3 pixels (Doulgeris, 2015). The final sea ice type maps have a pixel size of 40 REVI: m, but their

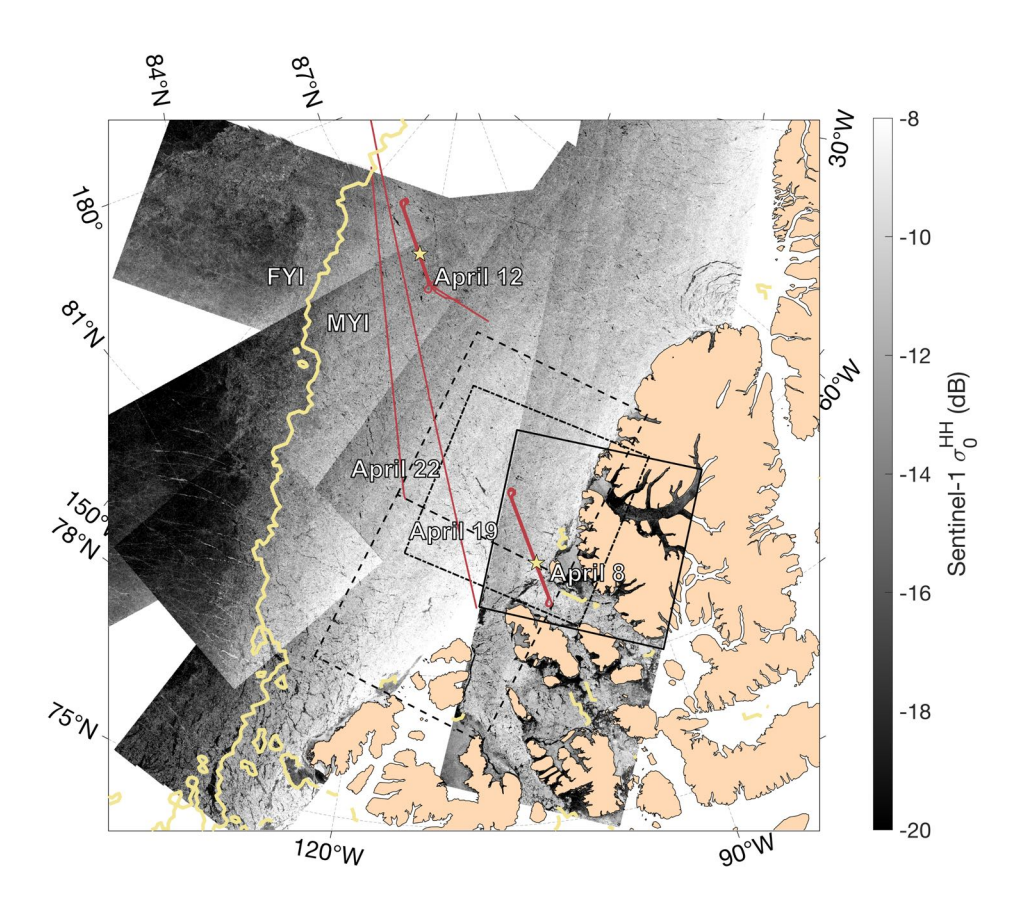


Figure 1. OIB campaigns during April 2019. S1 EW images collected around April 8th are shown in the background, with the black boxes outlining the images used for statistical analysis between C-band backscatter and sea ice freeboard. The solid box marks the boundary of the S1 image on April 8th, while the dashed (dot-dashed) ones mark those on April 7th (9th). The OIB ground tracks of the 4 days are marked by red lines, and the location of the *REVI:9 km* sample segments are shown by the asterisks. The thick yellow line delineates the boundary between the MYI and the FYI regions according to the sea ice type product provided by the Ocean and Sea Ice Satellite Application Facility (OSI-SAF).

effective spatial resolution is significantly coarser due to SAR speckle filtering and textural processing. Sea ice classification is carried out for all the S1 images and the results are used for further analysis.

By default, the S1 images are projected to $40^{REVI:}$ m spatial resolution, which is the nominal pixel spacing of the S1 EW medium GRDM mode data, though the effective resolution is approximately $90^{REVI:}$ m. In addition, the processing steps in SNAP may further degrade the resolution of the σ_0 map. This is because a Single Product Speckle Filter with a sliding window of 7×7 pixels wash applied during the speckle filtering process (Mansourpour et al., 2006). We use the following notations for the coarsened values: $\overline{F_s}^{(s)}$ and $\overline{\sigma_0}^{(s)}$, where s denotes the coarsening scale.

2.3 ICESat2 products

The official IS2 products (version 6) are accessed for the collocating tracks with OIB campaigns on April 8th and 12th (see Data Availability for details). Each of the beam segments are of about 150 aggregated photons, and the mean sea ice elevation of each segment is provided in ATL07. Due to the variable photon rates over the sea ice, the along-track length of the beam segment is not constant, around $10 \sim 16^{REVI:} m$. It is also different between strong and weak beams, with the beam segment length of the weak beams at about $50^{REVI:} m$. In this study, we use the footprints of both the strong and weak beam segments to study practical issues limiting the upscaling of IS2 measurements, extending our analysis from OIB to lower freeboard resolution $^{REVI:}$ but larger coverage.

130 2.4 Ancillary datasets

135

The climate data record of global sea ice drift from the Ocean and Sea Ice Satellite Application Facility (OSI-SAF, version OSI-455) is used as the reference to the collocation of the different datasets. The OSI-455 product is available for the period of 1991–2020, and is derived from various passive microwave sensors (SSM/I, SSMIS, AMSR-E, and AMSR2) and wind field data from an atmospheric reanalysis. The sea ice drift vectors are provided on the Equal-Area Scalable Earth (EASE) grid with the spatial resolution of 75^{REVI:} km. However, they are not available near the shoreline (i.e., part of the campaign on April 8th near the Canadian Arctic Archipelago). The temporal scale of the drift vectors is 24-hour, starting/ending at 12:00 UTC (Lavergne and Down, 2023).

2.5 Collocation between OIB and S1 images

The collocation between the F_s maps and σ_0 in the HH-polarization channel is carried out to correct for potential sea ice drift and geocoding uncertainties between the two measurements. REVI: The OIB flight on April 8th was approximately 40 minutes apart from its corresponding S1 image acquisition, whereas the OIB flight on April 12th was about 4 hours apart from its respective S1 image acquisition. For the OIB flight on April 8th, the ice surveyed was relatively immobile, while that covered by the campaign on April 12th experienced a drift of approximately $0.02^{REVI:}$ m/s according to the OSI-455 product. We coarsen the $1^{REVI:}$ m-scale F_s maps to the nominal pixel size of S1 EW images (i.e., $40^{REVI:}$ m), and maximize the correlation (Pearson's r) between the two fields by locally adjusting the relative location between the two. The increments of the local adjustments is

20^{REV1:} m (i.e., half of S1 EW pixel spacing). REV3: When collocating OIB tracks with S1 images, we divided the OIB tracks into 9 km segments. Collocation is performed independently for each 9 km outbound and inbound segment, in both the along-track and cross-track directions. In order to compare to the drift corrections during the correlation maximization(see Fig. 4.a and Fig. 5.a), the daily OSI-SAF drift vectors are scaled to the time interval between the acquisition time of the SAR image and that of the OIB. Afterwards, bilinear interpolation is carried out in the spatial domain to attain the drift vector at each location along the OIB flight path.

3 REV2: Methods

3.1 The statistical fitting between the F_s and σ_0

To analyze the statistical relationship between F_s and C-band backscatter, we employed a linear regression model for each 9 km segment (both outbound and inbound), defined as: $\overline{F_s} = a \cdot \sigma_0 + b$. Sea ice type maps, which classify the sea ice into LFYI, DFYI, and MYI, were used. During the classification, a sliding window of 11 pixels was applied in the classification process; if all pixels within an 11×11 window were of the same type, the central pixel was classified as a pure pixel (indicated by solid circles in Fig. 2 and 3, panel d-i); otherwise, it was labeled as a mixture(indicated by square symbols in Fig. 2 and 3, panel d-i). We specifically examined the relationship between F_s and backscatter for pure MYI pixels. Due to the limited number of pure FYI and DFYI pixels, these were not included in further analysis.

Backscatter values were binned into 1 dB intervals. For each bin, the mean F_s value within the interquartile range (IQR) was calculated. The representative backscatter value for each bin was determined as the mean of the bin boundaries. The statistical relationship between these mean F_s values and representative backscatter values was then analyzed.

Since the effective resolution of the backscatter used in this study is larger than $40^{REVI:}$ m, coarser spatial scales adopted for the computation of $\overline{F_s}$, including $100^{REVI:}$ m (Fig. 2, panel e and h) and $200^{REVI:}$ m (Fig. 2, panel f and i).

3.2 F_s distribution prediction

The prediction of F_s distribution is based on 1m-scale samples for OIB and beam-segment scale for IS2. The training of the prediction algorithm is carried out as follows:

- 1. Bins backscatter values into 1 dB intervals.
- 170 2. For each bin, calculates the mean F_s value within the IQR.
 - 3. Uses the three-component Log-Logistic mixture distribution to fit the F_s sample probability density function (PDF) within each σ_0 bin. The probability density function of the three-component Log-Logistic mixture distribution is given by:

$$p(x) = \sum_{i=1}^{3} \omega_i \cdot \frac{(\beta_i/\alpha_i)(x/\alpha_i)^{\beta_i - 1}}{(1 + (x/\alpha_i)^{\beta_i})^2}$$

where ω_i is the weight, β_i is the shape parameter, and α_i is the scale parameter for the *i*-th Log-Logistic component.

4. Applies the maximum likelihood estimation (MLE) method to fit the Log-Logistic mixture model. MLE identifies the optimal parameter estimates by maximizing the likelihood function of the sample data under the hypothesized Log-Logistic mixture distribution. We transform the problem of maximizing the likelihood function into minimizing the negative of the likelihood function. The sequential quadratic programming (SQP) algorithm is then used to solve this optimization problem.

To evaluate the goodness-of-fit between the sample distribution p(x) and the fitted three-component log-logistic mixture distribution $\widetilde{p}(x)$, we employed the Kolmogorov-Smirnov (K-S) distance, defined as:

$$\sup_{x} |P(x) - \widetilde{P}(x)|$$

Here, P(x) and $\widetilde{P}(x)$ denote the cumulative density function of the sample and the fitted distributions, respectively, and \sup_x the supremum of the difference between the two. The K-S distance ranges between 0 and 1, with higher value indicating larger discrepancy between the distributions. We further used the k-means algorithm for the clustering analysis of these components in all σ_0 bins, and related them to different sea ice types.

For the test of the prediction algorithm, we train the prediction model with the inbound segment, and carry out the prediction and validation on the corresponding outbound segment. For OIB tracks, the 9 km segment length is adopted, while for IS2, due to limited beam segment samples, the longer segment length of 27 km is adopted. For each σ_0 on the outbound segment, we use the fitted F_s distribution on the corresponding σ_0 bin on the inbound segment for the prediction. The predicted F_s distribution for each σ_0 sample is combined for all SAR pixels on the outbound segment. Finally, the prediction is validated by computing its K-S distance to the observed F_s distribution on the outbound segment. For comparison, the baseline for the validation is the K-S distance between the observed F_s distribution on the corresponding segment pair on the inbound and the outbound flight.

4 Results and analysis

175

185

190

4.1 Sample segments

We first examine two^{REVI:} pairs of 9 km OIB segments and collocate them with SAR images (σ_0 in HH-polarization), their locations shown in Figure 1. For the segment^{REVI:}s on April 8th, the mean F_s was $1.0^{REVI:}m$ with a standard deviation of $0.45^{REVI:}m$, and the mean σ_0 was $-10.46^{REVI:}$ dB with a standard deviation of $2.77^{REVI:}$ REVI: dB. In contrast, the segment^{REVI:}s on April 12th had a mean F_s of $0.57^{REVI:}m$ and a standard deviation of $0.18^{REVI:}m$, with a mean σ_0 of $-12.67^{REVI:}m$ dB and a standard deviation of $1.52^{REVI:}m$ dB. While the^{REVI:} 9 km segment^{REVI:}s covered on April 8th mainly consisted of thick MYI, that on April 12th features relatively thinner MYI, mixed with FYI and young ice.

4.1.1 Sample segment^{REVI}:s on April 8th

The first^{REVI:} 9 km sample segment^{REVI:}s is shown in Figure 2. The three OIB outbound flight passes are separated by about 75 minutes: 2019-Apr-8 12:34 (middle pass), 2019-Apr-8 13:48 (left pass), and 2019-Apr-8 15:01 (right pass), respectively. The inbound flight passes are: 2019-Apr-8 13:21 (middle pass), 2019-Apr-8 14:34 (left pass), and 2019-Apr-8 15:46 (right pass), respectively. For both the outbound and the inbound passes, the central pass overlaps with the left (or right) pass by approximately 100^{REVI:} m in the cross-pass direction. The collocation between the passes indicates minimum correction (1~2^{REVI:} m), very high correlations (Pearson's r over 0.95) and a decorrelation length of less than 5^{REVI:} m (Fig. S2).

For comparison, the collocation between the merged F_s map and the SAR image on the same day (details in Tab. B1) shows statistically significant but lower correlation coefficients (Fig. 2.b). The decorrelation length is much longer than that for $1^{REVI:}$ m-scale F_s (i.e. Fig. S2), mainly due to that correlation between F_s and σ_0 is carried out at the scale of $40^{REVI:}$ m. Besides, the statistical relationship between $\overline{F_s}$ and σ_0 in the HV-polarization channel is also significant $\frac{REVI:}{r}$, although the backscatter is weaker by more than 5 dB (Fig. S3)(details in Appendix C).

 $^{REV2:}$ As mentioned earlier, the effective resolution of the backscatter used in this study is coarser than 40 m. Therefore, larger spatial scales are also adopted for the computation of \overline{F}_s , i.e. 100 m (Fig. 2, panel e and h) and 200 m (Fig. 2, panel f and i).

As shown, the variability of $\overline{F_s}$ is drastically attenuated, but the statistical correlation between $\overline{F_s}$ and σ_0 (at original resolution) sharpens at larger scales. Specifically, for the segment on the outbound (inbound) flight, the Pearson's r increases from 0.61 (0.66) for the correlation at the $40^{REVI:}$ m-scale F_s to 0.81 (0.84) for that at the $200^{REVI:}$ m-scale F_s . For both cases, the slope of the linear fit also reduces slightly as the scale increases.

4.1.2 Sample segment^{REVI}:s on April 12th

210

220

225

The other two^{REVI:} 9 km sample segments are from the campaign on April 12th, shown in Figure 3. The major differences from the sample segments on April 8th (Fig. 2) are as follows: (1) according to the OIB F_s map, the MYI is much thinner; (2) it contains higher areal fraction of FYI, and (3) the surrounding sea ice has undergone more evident drift and deformation between the observations by OIB and S1, as indicated by the OSI-455 product.

Although sea ice is generally much thinner ($1^{REVI:}$ m-scale F_s mostly under $2^{REVI:}$ m), a statistically significant relationship is also present between $\overline{F_s}$ and σ_0 (Fig. 3 and Fig. C2). $^{REV2:}$ For comparison, we also applied a 2nd-order polynomial regression: $\overline{F_s} = a \cdot \sigma_0^2 + b \cdot \sigma_0 + c$. The nonlinear model yields slightly better fitting compared to the linear regression model (see Fig. S8 and S9). For both the outbound and the inbound segments, OIB has attained sufficient sampling of MYI, but the representation of FYI is not even. Specifically, on the outbound segment, SAR pixels with σ_0^{HH} under $18^{REVI:}$ dB are scarce, and no level FYI is detected in the area sampled by OIB. For the inbound segment, an apparent nonlinear relationship between $\overline{F_s}$ and σ_0 is observed for FYI, due to the effect of ice with different levels of development. LFYI has a consistently low $\overline{F_s}$ around $20 \ cm$ but corresponds to σ_0 that varies over a large range of $5^{REVI:}$ dB, whereas DFYI has strongly varying $\overline{F_s}$ up to around $1^{REVI:}$ m over a small range of σ_0 around $2\sim$ dB. The linear fitting for MYI is comparable to that for all sea ice types for the inbound flight (lower panels of Fig. 3). At both $100^{REVI:}$ m- and $200^{REVI:}$ m-scale, the linear regressions of $\overline{F_s}$ to σ_0 show lower fitting

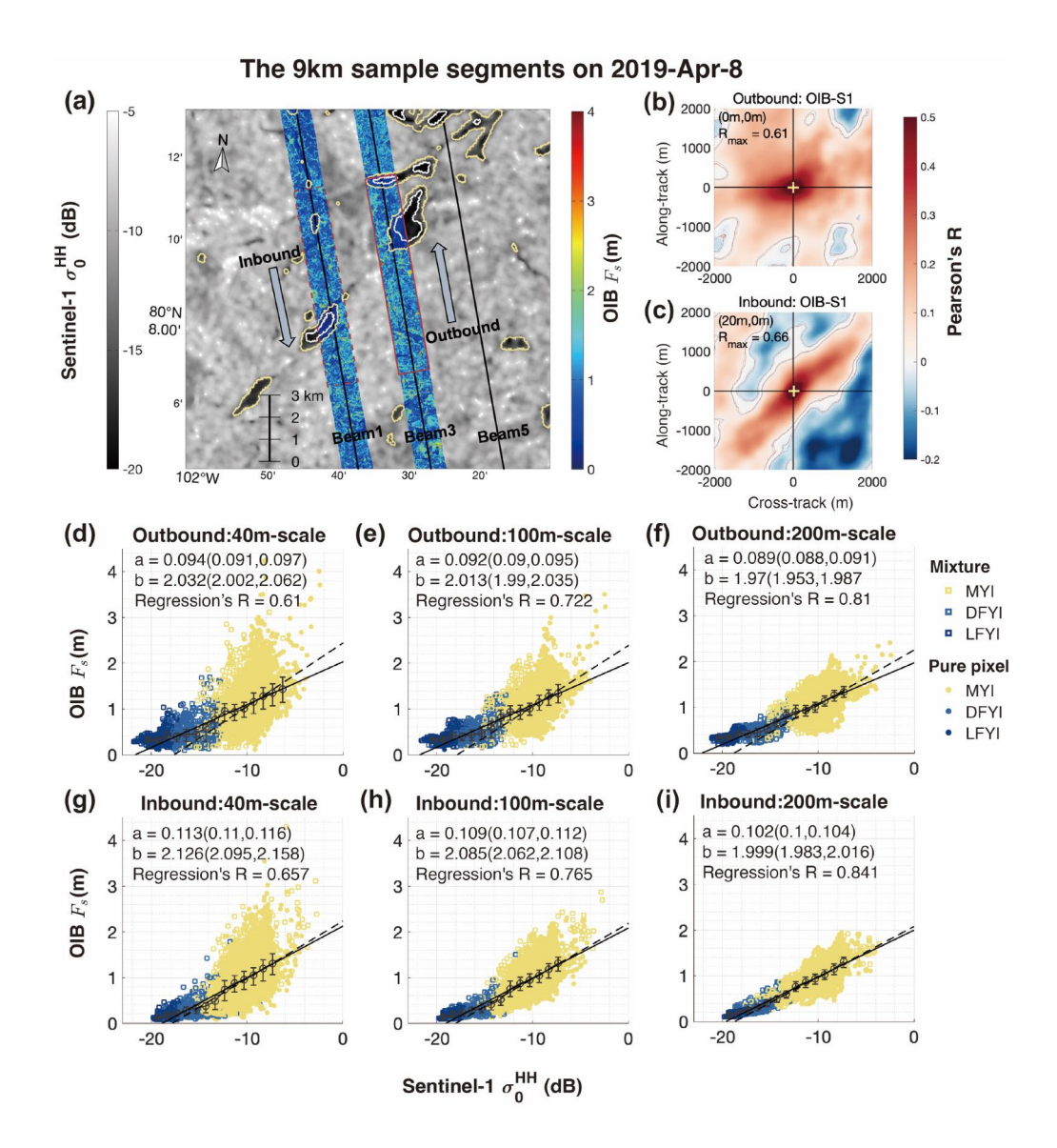


Figure 2. Total freeboard (F_s , colored) and the S1 HH backscatter (σ_0 , background) over sample segments on April 8th, 2019 (a). Contour lines delineate the boundary between different sea ice types, including MYI, level FYI (LFYI) and deformed FYI (DFYI). The ICESat-2 ground tracks of the three strong beams (#1, #3 and #5) are also shown as thin black lines. Two $^{REVI:}$ 10-km9 km segments on the outbound (i.e., northbound) and the inbound flights are marked out by the solid and dashed red boxes, respectively. $^{REV2:}$ The correlation map (Pearson's r) between σ_0 and F_s are shown with local corrections in 20 m steps in both the cross-track and the along-track direction (b and c). The yellow plus sign indicate the displacements to maximize the correlation between S1 and OIB. The scatter plots between $\overline{F_s}$ and σ_0 after collocation for the outbound (inbound) flights are shown in panels d, e and f (g, h and i). Three spatial scales for computing $\overline{F_s}$ based on the $1^{REVI:}$ m-scale F_s maps are adopted: $40^{REVI:}$ m (S1 image resolution, d and g), $100^{REVI:}$ m (e and h), and $200^{REVI:}$ m (f and i). In panels d to i, the dots are color coded according to their ice types, with the solid (dashed) lines showing the linear fitting lines of $\overline{F_s} = a \cdot \sigma_0 + b$ for all samples (only MYI pixels) and the fitted parameters. Also shown in each panel are the mean values of $\overline{F_s}$ and the $\frac{REV3:}{Interquartiles}$ $\frac{IQR}{IQR}$ after binning with σ_0 (1 $\frac{REVI:}{IQR}$ dB per bin).

slopes for MYI than for those based on all samples. The variability of F_s at 40-m scale diminishes considerably as the scale increases. In comparison, MYI always has much steeper regression lines for the sample case on April 8th across all analyzed scales (Fig. 2). This result, although potentially affected by the accuracy of the sea ice type map, highlights the importance of the sufficient sampling of various sea ice types to ensure their representation in the study of the statistical relationship.

Interestingly, for MYI which is well observed by both sample segments on April 8th and 12th, the statistical fittings between $\overline{F_s}$ and σ_0 show large differences. For the sample segment segment segment 8th, the regressions ($40^{REVI:}$ m-scale) are steeper at: $\overline{F_s} = 0.139 \cdot \sigma_0 + 2.443$ with Pearson's r = 0.410 (outbound) and $\overline{F_s} = 0.126 \cdot \sigma_0 + 2.236$ with the regression's R = 0.458 (inbound). In comparison, on April 12th, the fitting slopes are shallower by about 50%: $\overline{F_s} = 0.06 \cdot \sigma_0 + 1.338$ with the regression's R = 0.281 (outbound at $40^{REVI:}$ m-scale) and $\overline{F_s} = 0.051 \cdot \sigma_0 + 1.204$ with the regression's R = 0.263 (inbound). After binning the samples to σ_0 , the regression lines (i.e., between the mean values of F_s in each σ_0 bin and σ_0 's) become flatter on April 12th: $mean(\overline{F_s}) = 0.051 \cdot mean(\sigma_0) + 1.244$, compared with $mean(\overline{F_s}) = 0.105 \cdot mean(\sigma_0) + 2.123$ on April 8th. The potential causes of the different fittings include both: (1) differences in C-band backscatter sensitivity to macro-scale topography due to different ice/snow properties of the two regions, and (2) different imaging configurations of the SAR images.

4.2 Statistics of all segments on April 8th and 12th

235

250

255

265

For each of the $\frac{REVI:9}{m}$ OIB segment on April 8th and 12th, we generate a merged F_s map and collocate it with the SAR images on the same day. The statistical correlations are shown in Figure 4 and 5, respectively.

On April 8th, the local corrections for collocating F_s and σ_0 are all within 40^{REVI} : m (Fig. 4.a). The OSI-SAF drift product indicates about 100^{REVI} : m drift within the northern part of the OIB track, although the drift vectors are not significant given the respective product uncertainties. SAR images from the surrounding days (i.e., from April 7th and 9th, listed in Appendix B) also show little drift in the sea ice pack surveyed by the OIB campaign (details not shown). In addition, we have attained meterscale corrections for the collocation of OIB passes (see Fig. A1). Given the relatively coarser resolution of the SAR images, we assume that sea ice drift and deformation can be ignored when collocating F_s and σ_0 . The detected local corrections in Fig. 4.a may not indicate actual sea ice drifts, but may be due to geolocating uncertainties, such as those induced by geometric corrections of the SAR images. The correlation between $\overline{F_s}$ and σ_0 at 200^{REVI} : m scale is statistically significant for all segments (Fig. 4, panel b and d). After binning F_s samples to F_s to F_s the mean values of F_s and F_s

For the OIB campaign on April 12th, statistically significant large-scale sea ice drift are observed in the surveyed region (see Fig. 5.a). The lengths of the local corrections for collocating F_s and σ_0 are about 250^{REVI} m. The corrections are consistent between the local segment pairs on the inbound and the outbound flights, and they also agree with the large-scale drift in terms of both direction (north-east) and magnitude. Therefore, these local corrections correspond to the actual sea ice drift between the visits by the OIB campaign and S1.

After the corrections, the correlation coefficients are higher and statistically significant for all segments (p = 0.05 level). Moreover, the correlation coefficients after binning are mostly over 0.9 (Fig. 5, panels c and e).

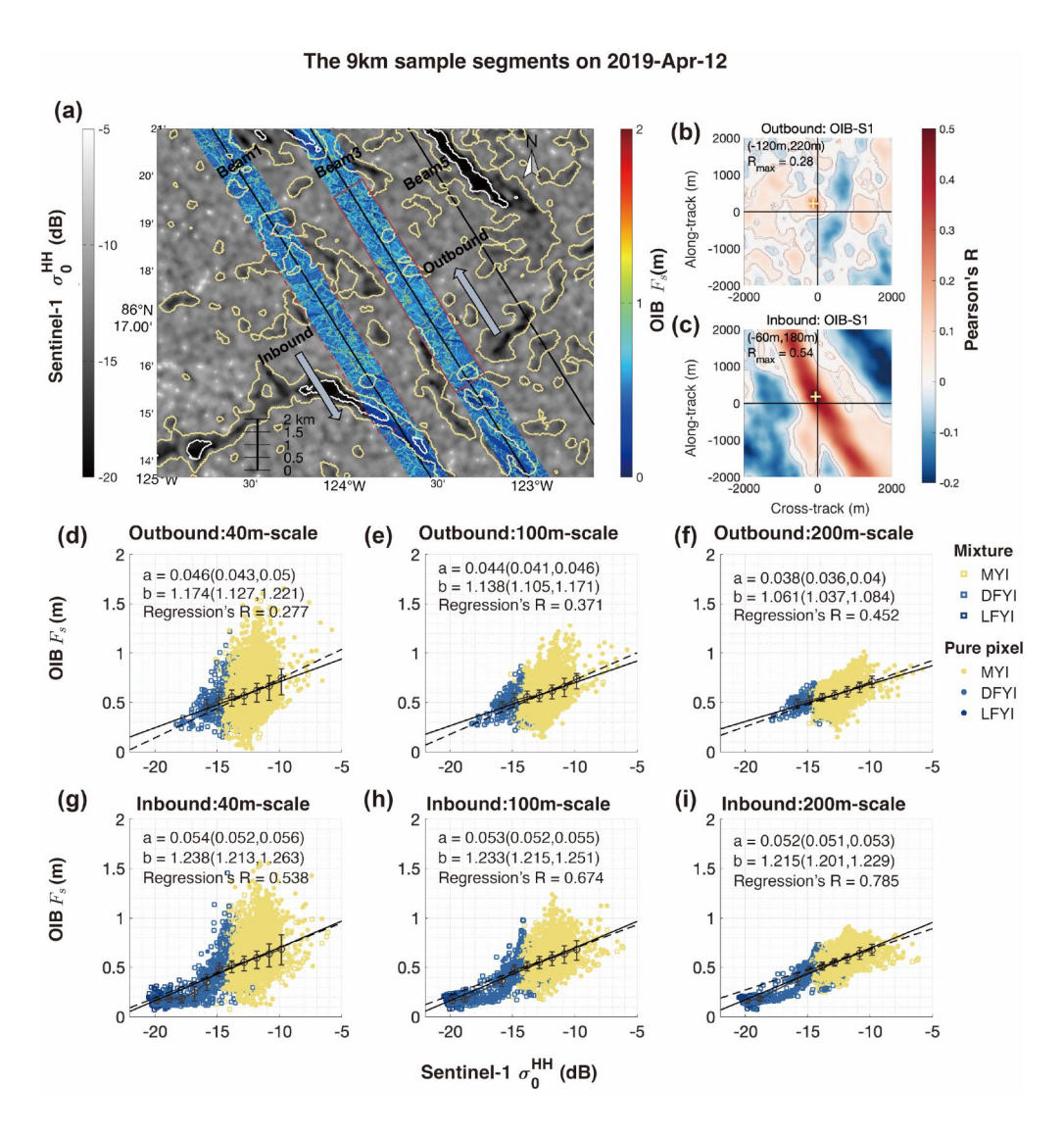


Figure 3. Same as Fig. 2, but for sample segments on April 12th.

In Figure 6 we show the linear regressions between σ_0 and $200^{\text{REVI:}}$ m-scale F_s for all segments on April 8th and 12th. The results indicate that with σ_0 and the regression relationships, we can estimate the $200^{\text{REVI:}}$ m-scale F_s with high statistical confidence (regressions' R-values over 0.3 for $\frac{\text{REVI:}}{\text{mostall}} 9^{\text{REVI:}}$ km segments). Furthermore, the regression parameters show significant variability among different segments, indicating the physical relationship between F_s and σ_0 varies locally. Despite this variation, the regression parameters from the inbound and outbound tracks are very similar. We further examine the relations for $27^{\text{REVI:}}$ km-long segments. As shown in Figure 6, the regression parameters for 27 km segments are much less variant, although certain variability still exists on different parts of the flight track. Specifically, for the segments on April 8th, the variance of a (b) has decreased by 48.6% (36.5%) when comparing $27^{\text{REVI:}}$ km-long segments to $9^{\text{REVI:}}$ km-long segments. For the segments on April 12th, the variance of a (b) decreased even more significantly, by 76.8% (78.7%). Besides, the regressions' R-values are also higher for $27^{\text{REVI:}}$ km-long segments for segments on both April 8th and April 12th. This implies that, small-scale inhomogeneity of the sea ice cover or errors in data co-location, which cause large variability of a's and b's in Figure 6, are effectively attenuated at larger scales. The regression relationships in Figure 6 can be further used for the prediction and construction of $200^{\text{REVI:}}$ m-sclae F_s maps based on SAR (Fig. S10 and S11). In particular, given to the locality of the relationships, the prediction of F_s map should also be carried out adjacent to the collocating observations by SAR and altimetic scans.

4.3 Prediction of F_s distribution with σ_0 map

Given that the altimetric scans by OIB (and IS2) have a finer resolution than available SAR images, the regression in Section 4.2 is inherently limited in the spatial resolution of the predicted F_s . Moreover, although there is a significant correlation between F_s and σ_0 , the variability of F_s is considerable, and no single predictor based on backscatter effectively captures this variability. Therefore, we focus on the prediction of meter-scale F_s distribution (i.e., at the full resolution of the altimeter data) with SAR images based on their collocating observations of F_s and relatively coarser σ_0 data.

4.3.1 Study of sample segments

275

280

285

290

295

We first study the REVI: 9 km sample segments in Section 4.1.1 and 4.1.2. REV2: Since the backscatter are binned at intervals of 1 dB, and then we perform statistical fittings of the 1 m scale F_s distribution for each 1 dB σ_0 bin. The distributions of F_s in typical σ_0 bins of these two REVI: 9 km sample segments are shown in Figure 7 and 8, respectively. The sample F_s distributions after binning all show the following characteristics. First, F_s follows a long-tailed, skewed distribution, which is consistent with various findings in existing studies (Xu et al., 2020; Duncan and Farrell, 2022). Second, REV3: there is strong heteroskedasticity associated with F_s : for larger σ_0 bins, the mean value and the variability of F_s are both higher. Third, the F_s distributions are multimodal, especially for σ_0 bins that contain both FYI and MYI samples (e.g., left panels in Fig. 7 and 8).

To capture the complex shape of the F_s probability density function (PDF), we use the three-component Log-Logistic mixture distribution to fit the sample PDF in each σ_0 bin. The fitting results (i.e., Fig. 7 and 8) indicate that the different PDF modes are well captured with very low $\frac{REV2}{Kolmogorov-Smirnov-(K-S)K-S}$ distance to the sample PDF. We further carry out clustering analysis of the various components, based on the modal F_s values and the corresponding σ_0 (right panels of Fig.

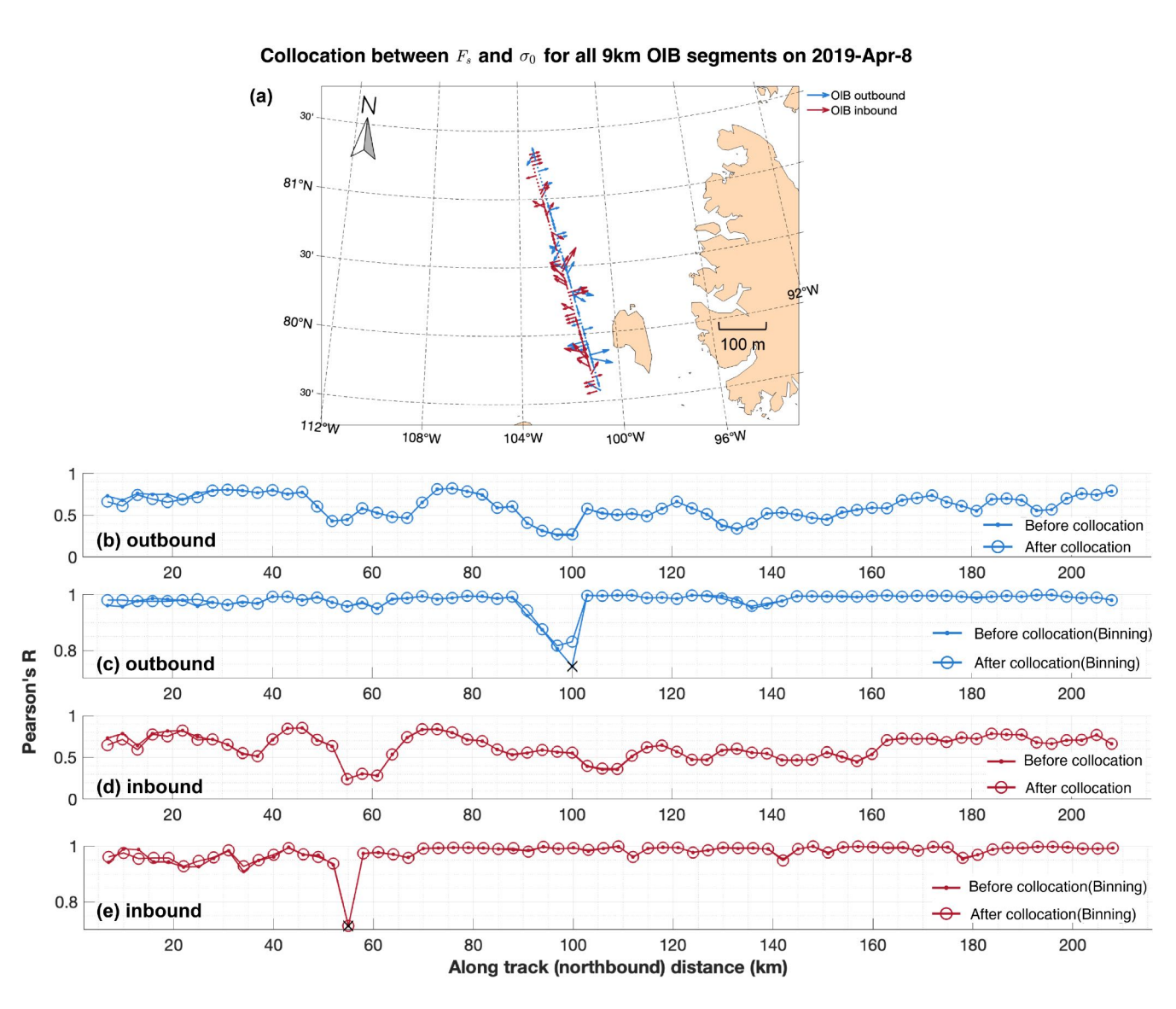


Figure 4. Statistical relationship between F_s and σ_0 for OIB segments on April 8th, 2019. The local corrections to maximize the correlation between $\overline{F_s}$ and σ_0 are shown for all segments with valid data on the outbound flight (blue) and the inbound flight (dark red). The correlation coefficients before and after collocation are shown for the outbound (panel b and c) and the inbound flights (panel d and e) for all segments, together with those after binning. Statistically insignificant correlations are shown by crosses (×) in the lower panels (p = 0.05 significance level).

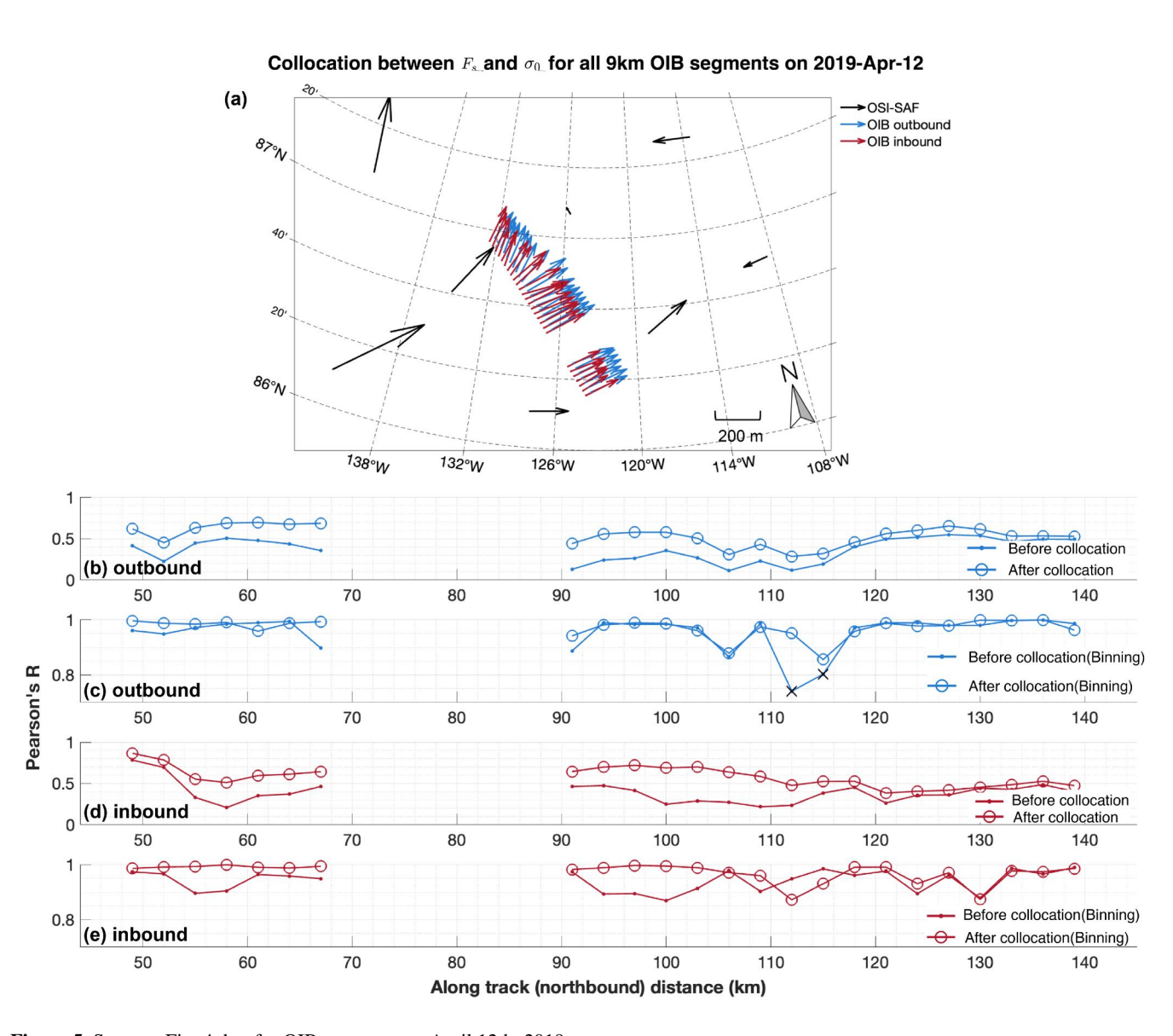


Figure 5. Same as Fig. 4, but for OIB segments on April 12th, 2019.

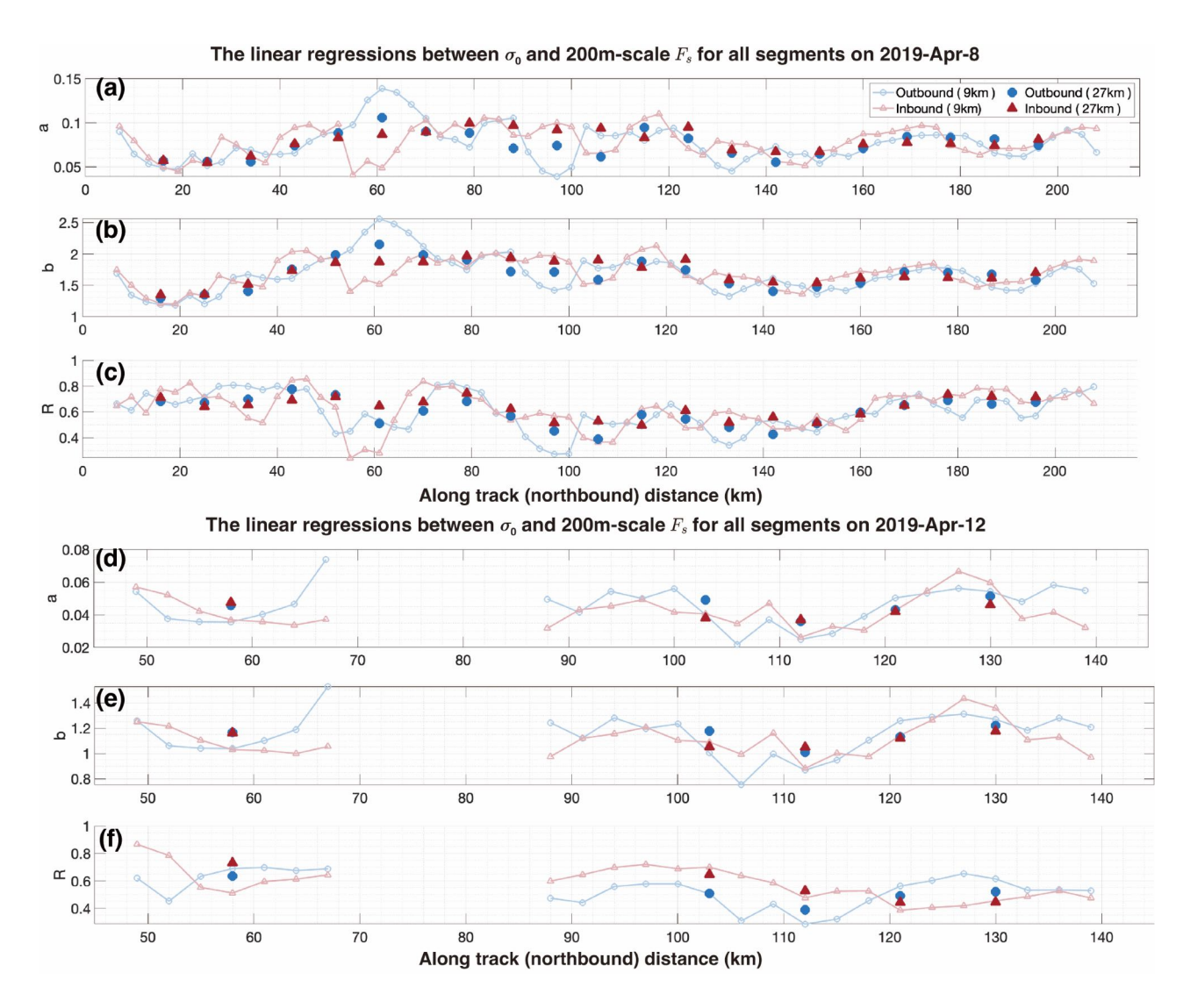


Figure 6. The linear regression from $40^{REVI:}$ m-scale σ_0 to the $200^{REVI:}$ m-scale F_s for all segments on April 8th (a, b and c) and April 12th (d, e and f): $\overline{F_s} = a \cdot \sigma_0 + b$. The regression's parameters, including a (panel a and d), b (panel b and e), and the R-value (c and f) are shown, respectively. Two segment lengths are adopted: $9^{REVI:}$ km and $27^{REVI:}$ km.

7 and 8). The three clusters indicate continuous changes of the PDF parameter with respect to σ_0 , and they generally show a good correspondence to these sea ice types: FYI, thin MYI and thick MYI. For example, for the sample segment^{REVI}'s on April 8th, there is prominent presence of MYI with F_s of over 3^{REVI} : m and σ_0 of over -5^{REVI} : REVI: dB (Fig. 7). This is captured by a separate Log-Logistic component which we manually categorize as the thick MYI. This could corresponds to sea ice of higher age than that of the thinner MYI which corresponds to the second component. Another example is that components with very small modal values of F_s manifest even at very large σ_0 bins (Fig. 7 and 8, lower panels). Due to the relatively coarse resolution of S1 images, thin FYI may be present in pixels with otherwise large values of both mean F_s and σ_0 . These components are captured by the PDF fitting, and we further manually categorize them as FYI. It is important to note that these categorizations are introduced to interpret the fitting results, as the specific categories (FYI, thin MYI, and thick MYI) were not previously defined in our analysis. Based on the per-bin F_s fittings on the inbound sample segments, we carry out the prediction of F_s distribution on the corresponding outbound segments. Specifically, based on the observed σ_0 map on the outbound segment, we: (1) formulate the distribution of σ_0 , (2) compute the F_s distribution according to the sample probability of each of the σ_0 bin, and (3) construct the overall F_s distribution on the outbound segment. For the REVI: 9 km sample segments on April 8th, the per-bin Log-Logistic mixture fittings demonstrate a high degree of accuracy in fitting the observations for both the inbound and the outbound segments, with K-S distances of 0.002 for each segment. However, the inbound and the outbound segments differ in the sample F_s distribution (Fig. 9.b), primarily attributed to variations in the thickness of FYI and MYI, as well as differences in their respective proportions. Notably, the modal thickness values of both the thin MYI and the thick MYI are $0.1^{REVI:}$ m higher on the outbound segment than on the inbound segment. As a result, the predicted F_s distribution also shows lower modal F_s values (Fig. 9.a). Despite the underestimation of the modal F_s , the prediction is closer to the observation, with lower K-S distance: 0.072, compared with 0.076 between the inbound and the outbound segment.

For the REVI: 9 km sample segments on April 12th, the prediction also shows lower K-S distance with the observed F_s distribution on the outbound flight (K-S distance from 0.094 to 0.074). The major improvement is due to different portions of thin FYI on the outbound and the inbound segments (see also Fig. 3). By using the σ_0 map on the outbound segment, we achieve the correct representation of thin ice in the predicted F_s distribution.

4.3.2 Validation of prediction for all segments

300

305

320

325

330

We carry out the prediction of $1^{REVI:}$ m-scale F_s distribution for all the $1^{REVI:}$ $9 \ km$ outbound segments. $1^{REVI:}$ The validation is based on the K-S distance between the observed F_s sample distribution and the predicted PDF. The baseline is the K-S distance between the observed samples on the inbound and the outbound segments. Figure 10 shows that the predicted F_s PDF is close to the observation, with the mean K-S distance at 0.077. There is a 10% reduction of the baseline K-S distance, which indicates that the predicted F_s distribution better matches the observations. Especially, large K-S distances are effectively attenuated with the prediction: 3 (10) out of the total $91^{REVI:}$ $9 \ km$ segments show a K-S distance over 0.15 between the predicted (inbound) F_s with the outbound observations. Moreover, there exists a significant positive correlation (Pearson's r: 0.72, p-value: 2.48×10^{-16}) between the K-S distance sequences in Figure 10. This indicates that when the F_s elevation is similar between the inbound and the outbound segments, the prediction is generally better. On the contrary, if the F_s distribution is more different between the two segments, the

The 9km sample segment on 2019-Apr-8 (inbound)

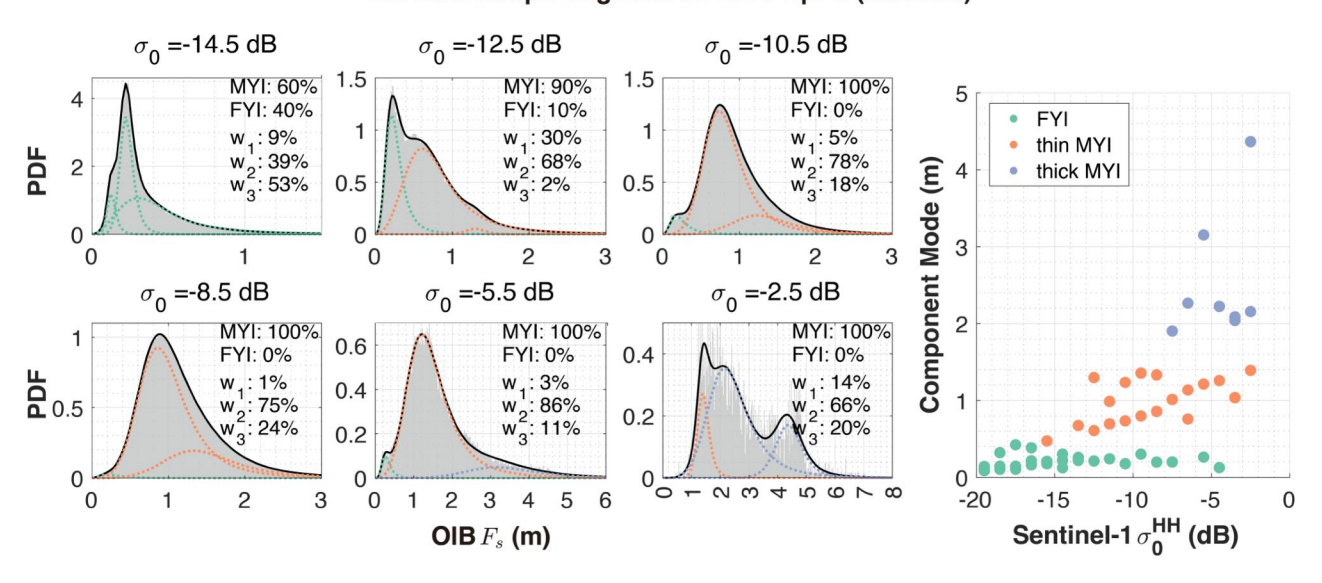


Figure 7. Distribution of 1^{REVI} m-scale F_s in typical σ_0 bins of the inbound sample segment on April 8th, 2019. F_s sample PDFs, as well as the fitted three Log-Logistic mixture components are shown for typical σ_0 bins (left panels). Statistical PDF fitting (black solid line) based on the 3-component Log-Logistic mixture model in each panel, along with each of the components (colored dash lines).

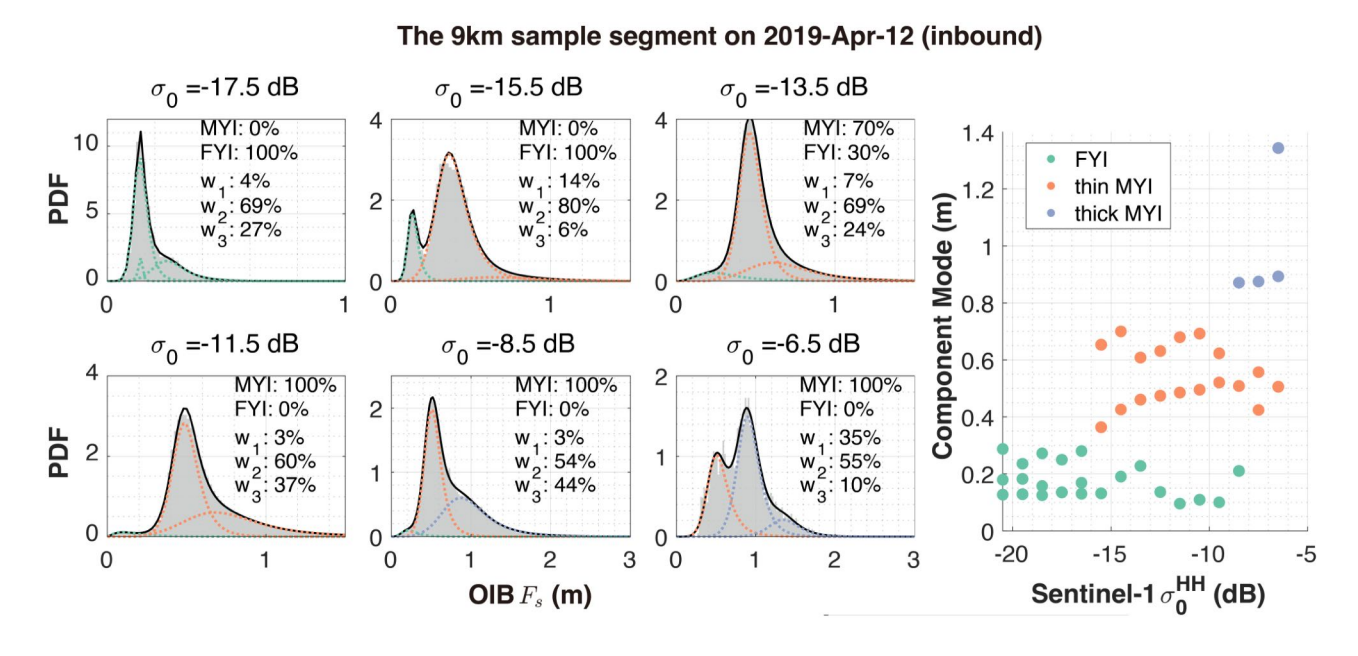


Figure 8. Same as Fig. 7, but for the inbound sample segment on April 12th, 2019.

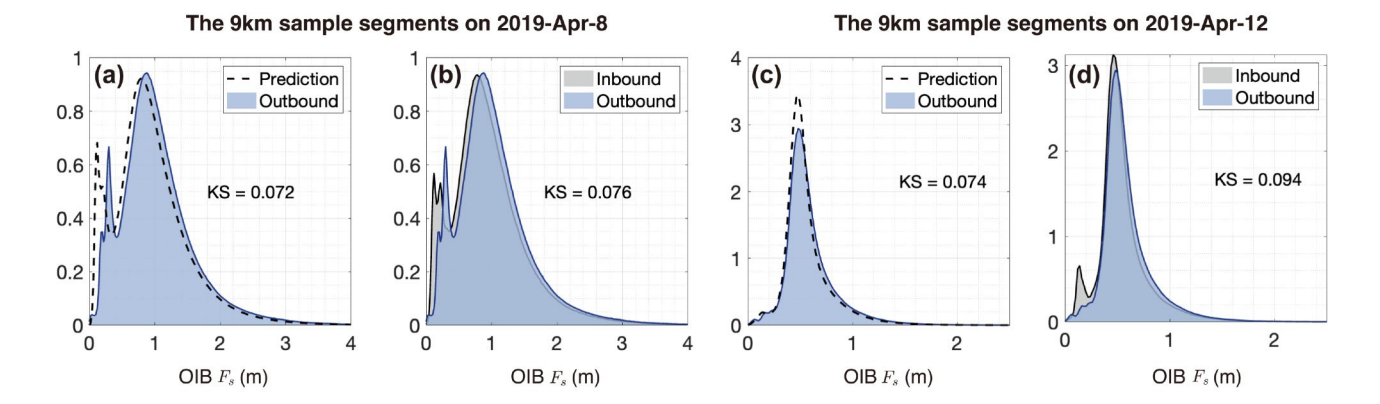


Figure 9. Statistical prediction of F_s distributions on the outbound segment with: (1) the per- σ_0 bin Log-Logistic mixture fittings on the corresponding inbound segment, and (2) the σ_0 map on the outbound segment. The observed and the predicted F_s distribution, as well as the K-S distance between the two are shown for the sample outbound segment on April 8th (panel a) and April 12th (panel c). The F_s sample distribution on the inbound and the outbound segments are also shown for comparison (b and d).

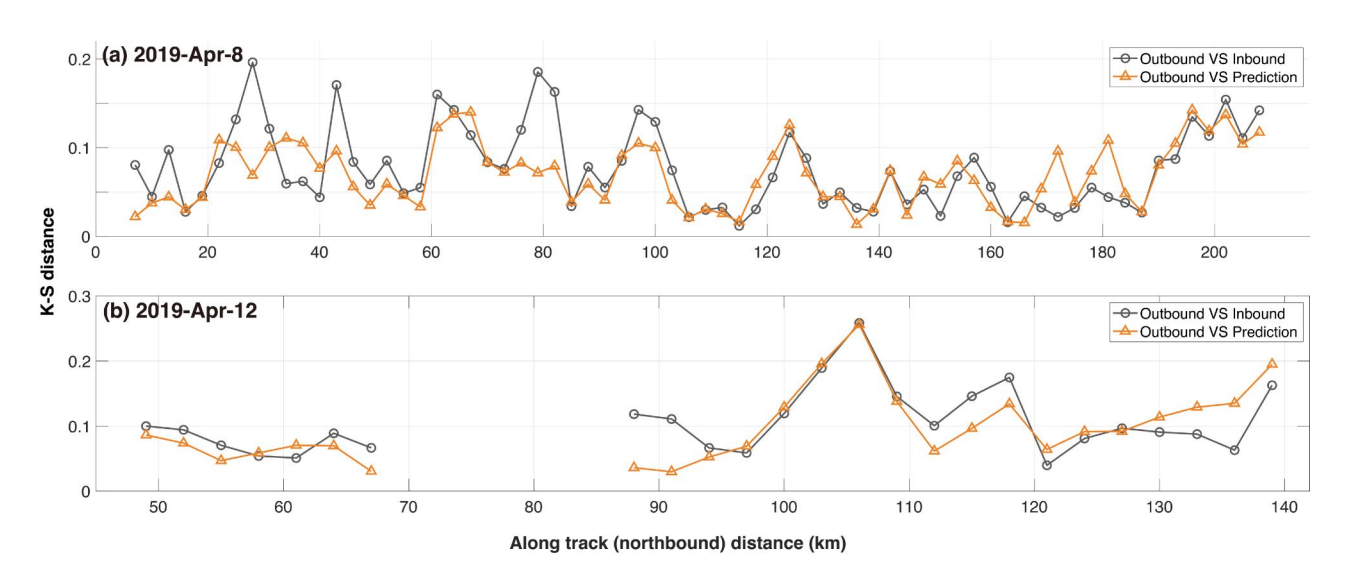


Figure 10. K-S distance between the predicted and the sample F_s distribution on all the $\frac{P_s}{9 \text{ km}}$ outbound segments on April 8th (top panel) and 12th (bottom panel). The prediction on each $\frac{P_s}{9 \text{ km}}$ outbound segment is carried out with the PDF fittings on the corresponding $\frac{P_s}{9 \text{ km}}$ inbound segment. The K-S distance between the inbound and the outbound sample F_s distributions are also shown.

prediction also deteriorates. Therefore, in order to obtain better predictions, the observed F_s should contain sufficient sampling of different sea ice types in the range of the prediction. Representation issues for large-scale retrievals are further discussed in Section 5.

5 Discussions and Summary

355

360

365

In this study we investigate the statistical relationship between sea ice freeboard and C-band microwave backscatter, by using collocated OIB observations and S1 images. Stronger SAR backscatter is observed for higher snow freeboard, which is attributed to the sensitivity of backscatter to both the sea ice type, with generally high volume scattering for MYI in winter, and ice topographic features such as ridges, with older ice having experienced stronger deformation (Krumpen et al., 2025). Moreover, the scale-dependency of this statistical relationship, along with its spatial and temporal locality, is further studied. An algorithm for predicting and extrapolating sea ice topographic measurements with SAR images is introduced that incorporates both: (1) the ICESat2 footprint size, and (2) the higher variability for larger sea ice total freeboard.

5.1 Physical mechanisms behind the statistical relationship between σ_0 and F_s

The statistical relationship between sea ice freeboard and C-band microwave backscatter is rooted in the different microwave backscatter mechanisms of various ice surface features. Thin, level ice typically exhibits low backscatter, with two primary scattering mechanisms contributing to this: surface scattering from the ice surface and volume scattering from air voids (Manninen, 1992). However, with thicker ice and larger F_s , both the backscatter and F_s variability are higher, as evidenced by the larger spread of F_s representatives \overline{IQR} in higher σ_0 bins in Fig. 2. This suggests that more complex physical mechanisms govern the C-band backscatter variations in thicker ice. In the case of older, rougher ice, the presence of thicker snow cover and more extensive ice deformation cause increased diffuse reflection and refraction of the incident radar signal (Onstott, 1992).

In addition to the wavelength-scale roughness, several other factors can also influence backscatter, such as the effective radar incidence angle, radar azimuth which are greatly affected by ridge geometry (Krumpen et al., 2025). For level ice, the effective incidence angle is relatively constant, equal to the radar incidence angle. However, for ridges, the local IA varies depending on the radar and ridge geometries, including the incident radar angle, the ridge slope, and the orientation of the ridge. Even with constant ice properties, these geometric differences alone can lead to higher surface backscatter from ridges compared to level ice (Manninen, 1992). Consequently, the radar backscatter and its IA dependency are highly dependent on the ice type and the observational geometry (Geldsetzer and Howell, 2023; Lohse et al., 2021, 2020; Guo et al., 2022).

It is important to note that in this study we did not apply IA corrections to the SAR images. There are several reasons: First, the IA dependency is type-dependent, with deformed ice showing lower sensitivity to IA than level ice (Makynen et al., 2003). Given the variant ridge density within the SAR's footprint ($\sim 100^{REVI:}$ m), a simple correction for IA is insufficient in our study. Second, for the SAR image on April 8th, the IA change was within 10° along the whole OIB track, and on April 12th, IA values were within 5° . Since the range of IA is small, the correction has potentially limited effect on our study. Third, the best angle for the IA correction should be chosen to maximize the differentiation among different ice types. What is the best angle remains an open question and requires more systematic study. We further explore the influence of IA on the statistical relationship for the OIB track on April 8th (no evident deformation or synoptic events around April 8th). By matching SAR images from April 7th, 8th, and 9th to the OIB track on April 8th, we obtain the statistical relationships between F_s at different IAs. In general, the statistical fitting becomes steeper with decreasing IA (Fig. S4). This trend is driven by the higher (lower)

sensitivity of σ_0 level (ridged) ice to changes in IA (note the weaker σ_0 's at larger IAs in Fig. S4). Therefore, when IA changes, the statistically significant relationship still holds, but IA has limited effect on this relationship than other factors, such as the localized sea ice conditions.

Furthermore, snow cover properties such as snow density and wetness can also modulate the C-band scattering signatures (Kim et al., 1984). For example, the change in snow density affects the effective wavelength of the microwave signals, therefore impacting the scattering at the snow-ice interface. Since the OIB campaigns were carried out during later winter/early spring, the snow cover is dry and therefore largely transparent to C-band signals. In order to apply the statistical prediction algorithm for other seasons (i.e., late autumn or spring), the snow conditions should be taken into account to better use the SAR measurements (Livingstone and Drinkwater, 1991).

5.2 Scale-dependency of the statistical relationship

380

385

390

395

Based on the OIB tracks on April 8th and 12th, we further explore the scale-dependent characteristics of the statistical relationship. Specifically, both F_s and σ_0 maps are coarsened to three spatial resolutions: $100^{REVI:} m$, $200^{REVI:} m$ and $500^{REVI:} m$. This coarsening was achieved by calculating the average values of F_s and the S1 intensity within each coarsening grid cell at the respective resolutions, rather than coarsening the OIB F_s alone as previously shown in Section 4. By analyzing the coarsened σ_0 and F_s maps, we find that the relationship becomes more stable at large scales (Fig. 11). In several F_s segments, the Pearson correlation coefficient at $500^{REVI:} m$ scale is lower than that at $40^{REVI:} m$ and $200^{REVI:} m$ scale. This is likely because FYI fraction diminishes for some segments after coarsening to the $500^{REVI:} m$ scale. On the OIB tracks on April 8th, there is a special segment ($55^{REVI:} km$ in along-track direction) where the Pearson correlation coefficient drops drastically across all three scales. These segments are dominated by deformed and thick ice, with a mean F_s of $1.04^{REVI:} m$, a F_s std of $0.56^{REVI:} m$, and MYI coverage reaching 97.3%. $8^{REVI:} m$ Moreover, the footprint size of NASA's first ICESat satellite is about 65m, and the statistical relationship with its concurrent SAR payloads (e.g., ESA's ENVISAT ASAR) can be explored for the prediction of large scale F_s .

Various studies have explored the relationships between sea ice topography and microwave backscatter on different scales, ranging from SAR-related scales (Macdonald et al., 2024; Kortum et al., 2024) to scatterometry scale (Petty et al., 2017). In Macdonald et al. (2024), the Radarsat Constellation Mission (RCM, also C-band SAR) images and ICESat-2 products are used to study the relationship between sea ice roughness and backscatter over land-fast sea ice in the Canadian Arctic Archipelago. In particular, the statistical relationship based on HV polarization is stronger, and therefore used to predict FYI roughness and the height of MYI. In our study, we also find statistically significant relationships on the HV channel (REVI: e.g., Fig. S3 and S5see Appendix C). Although the HV-channel usually has a lower SNR than the HH-channel, the higher correlations with sea ice topography statistics may arise from the higher dynamic range of σ_0 .

In Kortum et al. (2024) the authors explored the extrapolation of IS2 freeboard (ATL10) REVI: with temporally coincident S1 images., allowing for a time difference of up to 24 hours between S1 and IS2 measurements.

Similarly, in Macdonald et al. (2024), the HV-channel σ_0 maps are also utilized. The prediction is carried out with the pairing CDFs of F_s and σ_0 , and the Pearson correlation coefficient at $400^{REVI:}$ m scale reaches 0.82. In our study, the regression model in Section 4.2 can also be used to predict F_s maps at similar scales. To ensure consistency with (Macdonald et al., 2024;

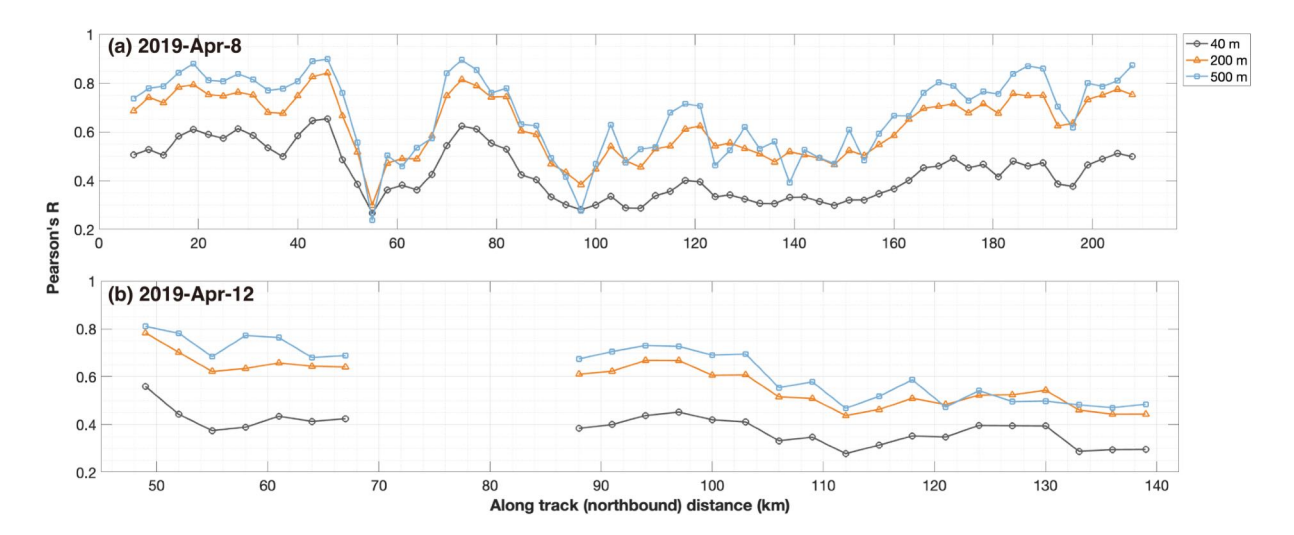


Figure 11. The statistical correlation between F_s and σ_0 at three spatial scales: $40^{REVI:}$ m, $200^{REVI:}$ m, and $500^{REVI:}$ m. The coarsening is applied to both F_s and σ_0 at these scales. The results for the OIB track on April 8th and 12th are shown in panel a and b, respectively. In order to accumulate enough samples, especially at the $500^{REVI:}$ m scale, both the inbound and the outbound segments are used to compute the correlation coefficients. Note that in order to accommodate the effective resolution of σ_0 maps, in Fig. 2 and 3, we only applied spatial averaging to F_s but not to σ_0 .

Kortum et al., 2024), REVI : we aligned the scale of statistical relationships and performed a quantitative analysis, with results presented in Tab. S1. However, compared to Kortum et al. (2024) and Macdonald et al. (2024), our study focuses mainly on the prediction of meter-scale F_s distributions (Sec. 4.3). In addition, we explored the effect of sea REVI : ice drift and deformation on the correlation between altimetric scans and SAR images. As shown in Section 4.2, third-party, large-scale drift products and local adjustments can be used to facilitate the collocation between the two. Related representation issues are further discussed in Section 5.3.

In Petty et al. (2017) the authors studied the statistical relationship between C-band backscatter measured by ASCAT and the variability of sea ice topography. The relationship is further used to estimate the atmospheric form drag coefficients based on backscatter maps. Although the scatterometers have relatively coarser resolution (25^{REVI:} km for ASCAT), the underlying mechanism of the topography-to-backscatter relationship is similar to our study. The macro-scale roughness of the sea ice cover (i.e., topography) and the sea ice type dependent surface properties affect microwave backscatter, resulting in the statistically significant relationship between the two.

415 5.3 Spatial and temporal locality of the statistical relationship between F_s and σ_0

405

The statistical relationships between F_s and σ_0 in Section 4.1.1 and 4.1.2 are based on OIB data and SAR images acquired on the same day. Furthermore, in Section 4.2, we demonstrated that there is large variability in this relationship, potentially caused by differences in sea ice/snow conditions and practical factors such as different observational geometries. Therefore,

the statistical relationship is spatially localized, which implies that the extrapolation of freeboard measurements (e.g., Sec. 4.3) should be carried out locally.

Furthermore, we explore the temporal transferability of this relationship, by matching SAR images collected 1 week from the OIB campaigns. Correspondingly, sea ice may undergo significant drift and deformation, as well as thermodynamic changes during a week-long interval between the OIB and SAR observations.

For the F_s sample segment F_s on April 8th (Sec. 4.1.1), we use SAR images from April 1st and April 15th, and collocate both with the F_s map on April 8th (Fig. S5). The analysis of the drift corrections indicates that there is negligible sea ice movement between April 8th and April 15th, and the statistical relationships between F_s and σ_0 are consistent (Fig. S5, lower panels). However, the maximum correlation coefficient between F_s and σ_0 is much lower at 0.4 for the SAR image on April 1st, as compared to 0.6 for April 8th (Fig. S5, upper panels). The drift corrections obtained from SAR images on April 1st and April 8th confirm significant sea ice deformation, leading to suboptimal collocation between not only SAR images, but also SAR and OIB (note the scattered samples in Fig. S5, panels b and c).

For the $^{REVI:}$ 9 km sample segment $^{REVI:}$ s on April 12th (Sec. 4.1.2), SAR images from April 5th and April 19th are used for a similar analysis. Between April 5th and 12th, significant sea ice drift and deformation is present for the sea ice cover around the sample segment $^{REVI:}$ s (Fig. S6.a). Correspondingly, the correlation coefficients between F_s and σ_0 also witness significant drops: from 0.28 to 0.15 for the outbound segment, and from 0.54 to 0.45 for the inbound segment. On the contrary, between April 12th and 19th, sea ice drift is evident, but very small deformation is present, as indicated by the collocation of SAR images (Fig. S6.d). The correlation coefficients between F_s on April 12th and σ_0 on April 19th largely remain the same as that based on April 12th. Specifically, the coefficient is 0.27 for the outbound segment and 0.54 for the inbound segment.

Both cases indicate that the collocation between OIB and SAR deteriorates at longer time intervals, and there are corresponding drops in the statistical relationships. This is presumably caused by synoptic scale forcings that drive sea ice drift and deformations, which compromise the collocation. As indicated by both observations and modeling studies (Marsan et al., 2004; Rampal et al., 2008; Ning et al., 2024), sea ice deformation is localized, and multi-fractal both spatially and temporally. More importantly, there is strong coupling between the spatial and the temporal domain. At longer time intervals, there is lower spatial localization of sea ice deformation, which potentially complicates the collocating of SAR and altimetry scans. Furthermore, thermodynamic changes such as snowfall events, snow stratigraphic changes, as well as newly formed sea ice ridges and leads, can also greatly modulate both F_s and/or C-band backscatter(Tsai et al., 2019; Manninen, 1992). These changes are usually associated with synoptic events, which potentially co-occur with sea ice drift and deformation. In summary, there is a strong locality in the statistical relationship between F_s and σ_0 . The spatial and temporal windows for collocating SAR and altimetry scans and further upscaling the freeboard measurements is an important research topic for future studies.

5.4 On the upscaling of IS2 measurements

420

425

430

435

440

445

Compared with the $1^{REVI:}$ m-scale F_s maps from OIB, the standard sea ice elevation (ATL07) and freeboard (ATL10) products of IS2 are provided in beam segments. Since each beam segment consists of ~ 150 aggregated photons, the nominal resolution is between 10 and $20^{REVI:}$ m in the along-track direction for the three strong beams and ~ 11 m in the across-track direction,

the laser footprint's diameter (Neumann et al., 2020). For weak beams, the beam segment resolution is even coarser by approximately 4 times. By constraining and coarsening OIB F_s maps to the footprints of IS2 strong and weak beam segments, we find that the correlation maps between F_s and S1 backscatter is in good agreement with those based on the full OIB segment (results for the sample segments shown in Fig. S7). Therefore, the collocation with S1 images can also be carried out with IS2 elevation measurements.

We re-apply the prediction algorithm in Section 4.3 to IS2 footprints of the $REVI: 9 \ km$ sample segments. Specifically, the prediction is trained and validated on the IS2 beam segments on the inbound and the the outbound OIB segments, which cover the IS2 beam pairs #1-#2 and #3-#4, respectively. However, compared to the $1^{REVI:} m$ -scale OIB F_s map, the following limitations of IS2 are present: First, the IS2 beam segments are coarser, especially for the weak beams. Second, the IS2 ground coverage is much narrower at $11^{REVI:} m$, compared with the $\sim 1.5^{REVI:} km$ width of the F_s map. As a result, on the $9^{REVI:} m$ sample segments, there is a very limited number of IS2 beam segments (i.e., $\overline{F_s}$ samples). Therefore, in order to accumulate enough samples for prediction, we extend the sample segments in both directions to $27^{REVI:} km$ (equivalent to the length scale used in Fig. 6).

Specifically, we follow the three-step routine for the prediction and evaluation of F_s . First, by using IS2 beam segments on the inbound segment (i.e., the #1-#2 beam pair), we bin the F_s samples to σ_0 , and further carry out the PDF fitting with 3-component Log-Logistic mixture model within each σ_0 bin. Second, we predict the F_s distribution on the corresponding outbound segment, using the σ_0 observations on the IS2 footprints (i.e., the #3-#4 beam pair). Finally, we validate the prediction with the observed F_s samples.

Figure 12 shows the results for the $^{REVI:}$ $\underline{27~km}$ sample segments on April 8th and 12th. Similar to the validation of the $1^{REVI:}$ m-scale F_s in Figure 9, the prediction on IS2 footprint also yields a good match with the observed F_s distribution. In addition, the K-S distance is effectively reduced with the prediction: from 0.189 to 0.123 for the sample segment on April 8th, and from 0.182 to 0.119 for that on April 12th. Using the σ_0 map on Beams #3 and #4, we produce the F_s distribution that better matches the observation than the default F_s distribution on Beams #1 and #2. Especially, the representation of thin ice (less than $30^{REVI:}$ cm thick) has greatly improved for both cases, which is the major reason for the reduction in the K-S distance.

REV3:

455

465

470

480

485

For future work, we plan to further explore the freeboard-backscatter relationship under various conditions. First, a more extensive coverage of sea ice types is planned, including FYI and thin ice at different stages of development. The historical records of OIB in the Arctic contain many surveys over various ice conditions especially in the western Arctic. The concurrent SAR campaigns including S1 can be used to extend the study with more complex ice types and mixtures. Second, the statistical relationship and its variability under different weather conditions need more investigation. Factors such as melt conditions and heavy snowfall could potentially alter both the microwave backscatter and the overall snow budgets. As pointed out in Section 5.3, we need to account for potential changes in the sea ice under synoptic events, and further obtain the optimal spatial and temporal window to derive the relationship and the upscaling of altimetry measurements.

For the upscaling of IS2 observations at basin scale, concurrent and spatially collocated SAR images should be used, such as those from S1 and the RadarSat Constellation Mission (RCM, see: MDA, 2021). Specifically, we have demonstrated both

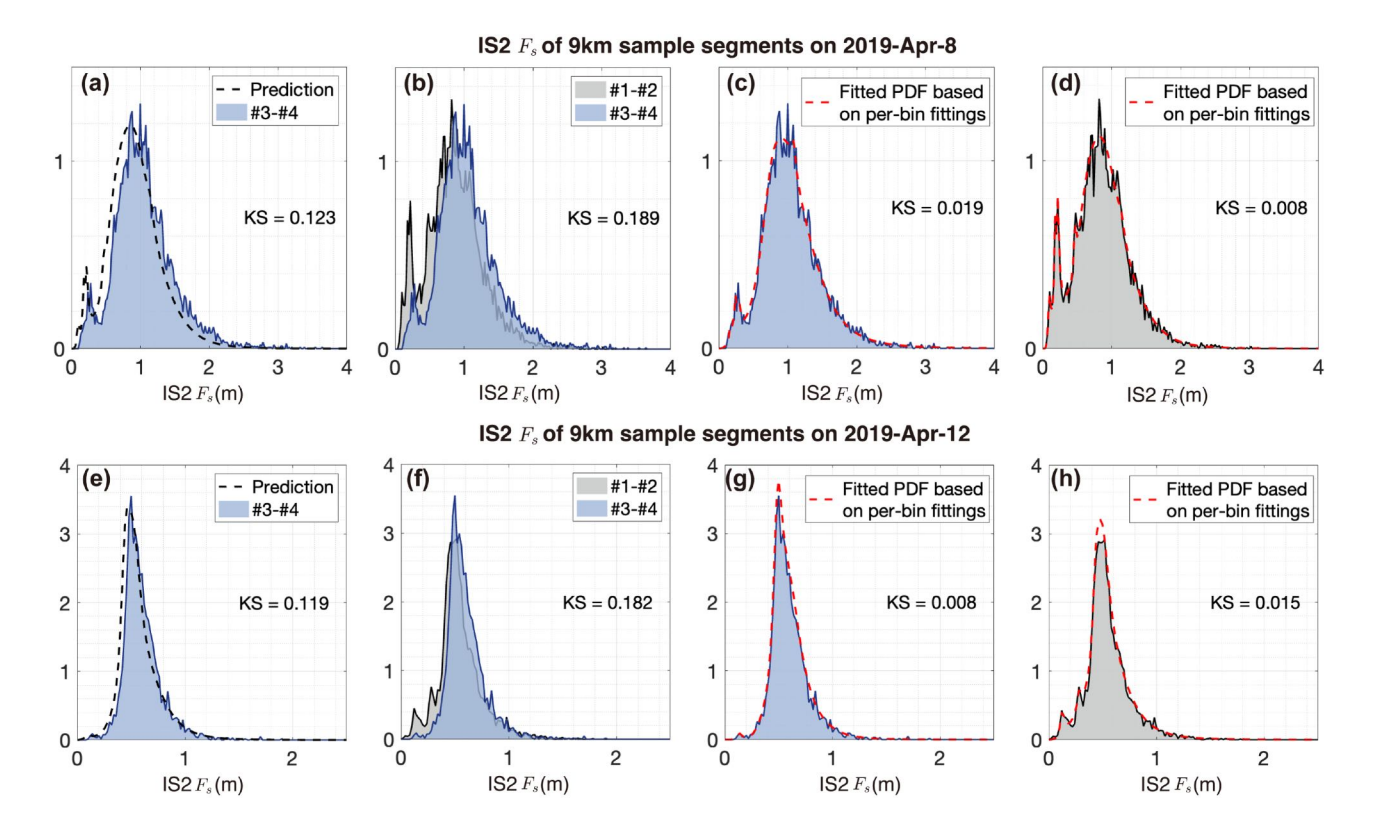


Figure 12. Same as Fig. 9, but for F_s on IS2 beam segments on the sample segments on April 8th (panel a and b) and April 12th (panel c and d). Since there are limited number of IS2 beam segments, the length of the sample segments is enlarged to $27^{REVI:}$ km.

spatial and temporal locality of the derived statistical relationships. For altimetry and SAR observations that are separated by long temporal intervals, thermodynamic and dynamic processes within the ice and overlying snow can degrade the relationships between macro-scale topography and C-band backscatter. Another key factor is the spatial scale for the upscaling of IS2 measurements. In Section 4.3 the prediction is designed to incorporate meter-scale F_s maps. REV3: The photon-based elevations represent a similarly fine spatial scale to the OIB ATM, but contain also be accounted for. The photon-level elevation measurements represent a similarly fine spatial scale to the OIB ATM, but contain higher uncertainty than that of the beam segment elevations (ATL07). The proper temporal and spatial scales for matching SAR images and upscaling of IS2 measurements should be the subject of detailed studies in the future.

490

500

The sea ice topographic roughness and the statistical fittings are dependent on the scale of altimetric observations (Sec. 4). Beyond the OIB ATM scans ($1^{REVI:}_{m}$ -scale) and the IS2 beam segments ($1^{REVI:}_{m}$ -scale) and for the strong beams footprint size 1 m, various historical and future campaigns feature drastically different payload design and resolutions. For example, the nominal footprint size of ICESat is $65^{REVI:}_{m}$ (Farrell et al., 2009), and at this scale there also exist statistically significant relationships between 1 m and the C-band backscatter (Kortum et al., 2024; Macdonald et al., 2024). Besides, the concurrent SAR observations at both C- and L-bands, such as ALOS (Advanced Land Observing Satellite) and ALOS-2 (Shimada et al.,

2009; Kankaku et al., 2013), can be further used for the study of the relationships and the upscaling of altimeter measurements. For ICESat, by combining with data from SAR satellite payloads such as ESA's EnviSat ASAR (Miranda et al., 2013), the upscaling of ICESat can be carried out for constructing a wider coverage record of sea ice freeboard for the period 2003–2008.

Data availability. The data from OIB campaigns in April, 2019 are available from the National Snow and Ice Data Center: https://nsidc.org/data/ilatm1b/versions/2, and https://nsidc.org/data/ilnsa1b/versions/2 (last access: 6 September 2024). S1 EW images are accessed from the Copernicus Data Space Ecosystem (available at https://browser.dataspace.copernicus.eu/, last access: 6 September 2024) and processed them using the ESA Sentinel Application Platform (SNAP) toolbox. The complete list of used SAR images are provided in the supplement with public access. The ATL07 and ATL10 product from ICESat-2 (version 6) are accessed at the National Snow and Ice Data Center through https://nsidc.org/data/atl07/versions/6 and https://nsidc.org/data/atl10/versions/6 (last access: 6 September 2024). The OSI-SAF sea ice drift product is available at: https://osi-saf.eumetsat.int/products/osi-455 (last access: 6 September 2024). DTU15MSS_1min can be found at: https://www.space.dtu.dk/ (last access: 12 February 2025).

The interpolated and stitched 1^{REVI}: m-resolution total freeboard fields (in 3^{REVI}: m segments) of the sample segments on 2019-Apr-8 and 2019-Apr-12 are achieved at: https://zenodo.org/records/14930672 (last access: 26 February 2025). Additionally, the sea ice type maps based on Sentinel-1 EW images can also be accessed at the same URL.

Appendix A: Processing of OIB ATM elevations

515

520

525

530

The elevations of the original ATM samples are converted into the total freeboard (or the snow freeboard, denoted F_s). For OIB flights on April 8th and 12th which were organized $\frac{REVI}{into-racetracksin}$ a racetrack pattern (Fig. 1), we merge all OIB samples to construct a merged map of F_s for both the northbound and the southbound flight passes. Specifically, two steps are carried out, as follows.

A1 Construction of the per-pass $1^{REVI:}$ m-scale F_s map

As the first step, for each OIB pass, we converted OIB ATM samples into the F_s map which covers over $500^{REVI:}$ m across the OIB flight path. Both wide scan and the narrow scan of the OIB ATM are utilized. For a local segment along the OIB flight (e.g., $10^{REVI:}$ m in length), we first project each ATM sample under the polar stereographic projection according to its geolocation (i.e., its latitude and longitude). Then, we interpolate the samples into a $1^{REVI:}$ m-scale elevation map, using linear interpolation. $^{REV3:}$ Afterwards, we apply atmospheric and tidal corrections to the elevation based on mean sea-surface height (DTU15 MSS model). Afterwards, we apply mean sea surface (MSS) geophysical height corrections to the elevation based on mean sea-surface height (DTU15 MSS model). Finally, we treat the corrected elevation as elevation anomalies, and apply the lowest elevation method to retrieve the freeboard. Specifically, the lowest 1% of elevation samples within each $10^{REVI:}$ m segment are extracted and linearly interpolated to construct the local water level (also at $1^{REVI:}$ m-scale) using the Inverse Distance Weighting (IDW) method. The final $1^{REVI:}$ m-scale F_s map is further validated with the standard $40^{REVI:}$ m-scale F_s product from IDCSI (Fig. S1).

A2 Collocation between OIB passes and the construction of the merged F_s field

535

540

545

555

560

We further merge the three OIB passes to form the F_s map that covers over $1.4^{REVI:}$ km across the flight path. Since the central pass and the left pass were separated by $1\sim2$ hours, and the central pass and the right pass by $3\sim4$ hours, the sea ice cover potentially had undergone drift and deformation. Therefore, we first search for corrections between each of the two pairs of OIB passes. For each $3^{REVI:}$ km segment, we maximize the correlation of the overlapping part of the F_s maps of the central and the left (or the right) pass, by adjusting the relative location of the left (or the right) pass with respect to the central pass. After the maximum correlation is attained, we record the corrections in both the along-track and the cross-track directions, and further merge the left and the right pass to the central pass, in order to form a unified F_s map. In Figure 2.a (3.a) we show the merged F_s maps for the sample segment F_s on April 8th (12th), and in Figure S2 (S3) the correlation maps between OIB passes.

For certain segments, the central pass and the left (or right) pass do not overlap, and therefore they are not included in further analysis (especially in Fig. 5). Figure A1 and A2 show the corrections and the maximized correlation of F_s maps between OIB passes for all $3^{REVI:}$ km segments on April 8th and 12th, respectively. For April 8th, very high correlation coefficients were attained for all segments (Pearson's r all over 0.94). Besides, meter-scale corrections were required, which potentially arise from locating uncertainties. On the contrary, on April 12th, evident corrections with length over $100^{REVI:}$ m were needed to maximize the correlation, which are also consistent with the large-scale drift provided by OSI-SAF (details not shown). Therefore, we consider these corrections are associated with sea ice drifts. Evident changes of the sea ice drift at the location of $120^{REVI:}$ km along the OIB flight path is detected for both the inbound and the outbound flights, indicting the presence of sea ice deformation. Especially, the correlation coefficients for the $3^{REVI:}$ km segments also dropped to lower than 0.9 where the deformation is detected. Collocation and the resulting correlation coefficients at the scale of $500^{REVI:}$ m around the location of of the deformation further indicate that the deformation are localized (i.e., within $500^{REVI:}$ m) and present at several along-track locations (Fig. A2).

Appendix B: S1 EW images used for analysis for OIB campaigns

REV2: The sea ice classification algorithm used in this study is based on: Lohse et al. (2020, 2021); Guo et al. (2023). Lohse et al. (2020) developed a supervised algorithm that accounts for the class-dependent IA effects, known as the GIA classifier. While this classifier performs well in addressing IA sensitivity, some misclassifications and ambiguities remain. To address these issues, Lohse et al. (2021) and Guo et al. (2023) enhanced the algorithm by incorporating GLCM texture features, resulting in improved class separation. This study uses this classification approach to produce sea ice type maps on the selected S1 scenes.

In the classification process, seven GLCM textures are derived from the HH-channel of each SAR image, with a texture window size of 11 pixels. Then, SAR intensities (HH and HV) and GLCM textures (HH) are used as input to the GIA classifier, which incorporates their IA dependencies. Sea ice is classified into three types: level first-year ice (LFYI), deformed first-year ice (DFYI), and multiyear ice (MYI). To further refine the results, a Markov Random Field based contextual smoothing process is applied with a window size of 3 pixels (Doulgeris, 2015). The final sea ice type maps have a pixel size of 40 m, but their effective spatial resolution is significantly coarser due to SAR speckle filtering and textural processing.

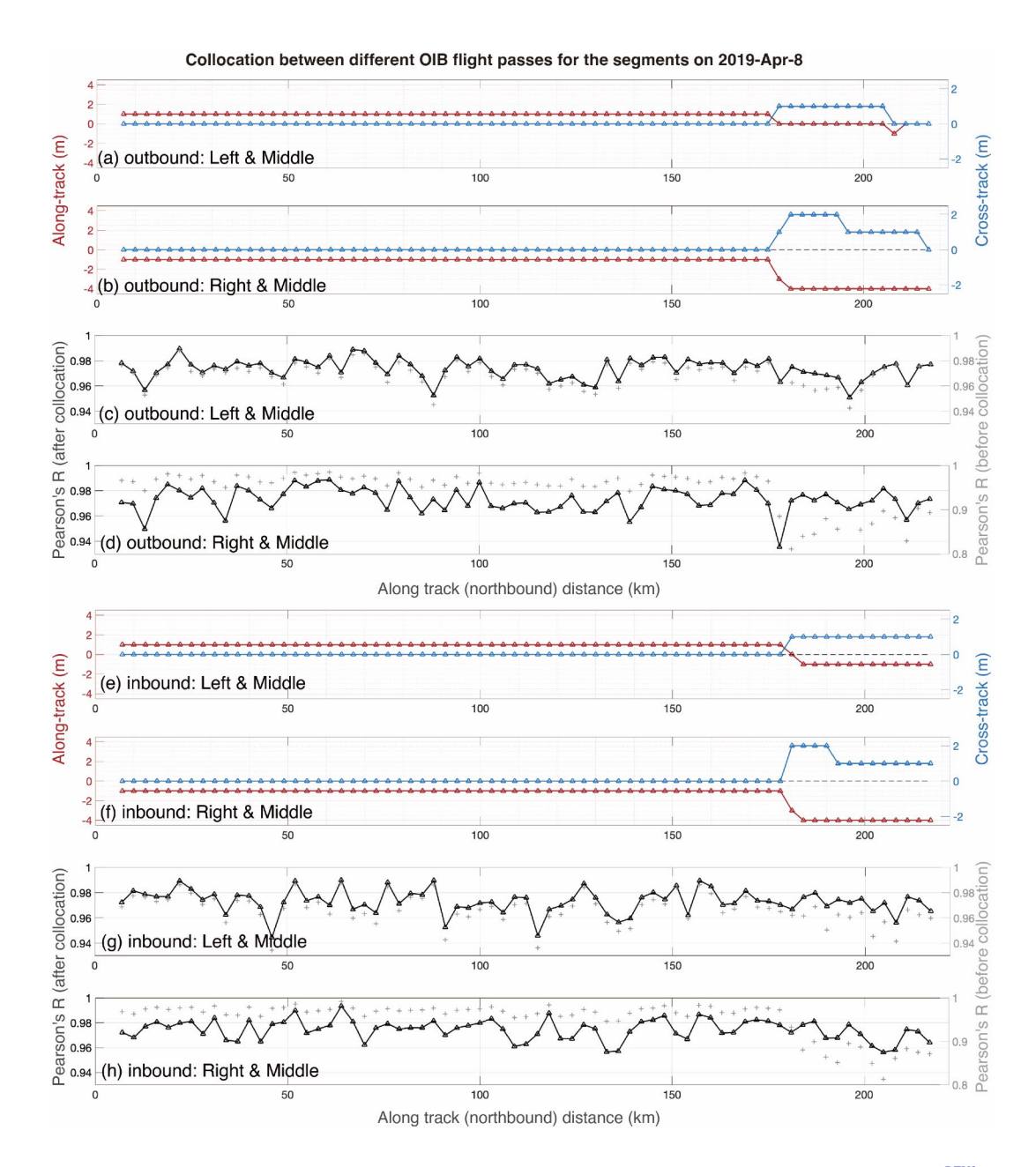


Figure A1. Collocation between different OIB flight passes on April 8th, 2019. The along-track segment length is 3^{REVI} _km. The local corrections of the left and the right pass with respect to the middle pass for each segment on the outbound (inbound) flights is shown in panel a and b (g and h), respectively. The correlation coefficients (Pearson's r) after the collocation between the left and the middle pass and that between the right and the middle are shown in panel c and d the for the outbound flight, respectively. Similarly, panel e and f show the results for the inbound flights.

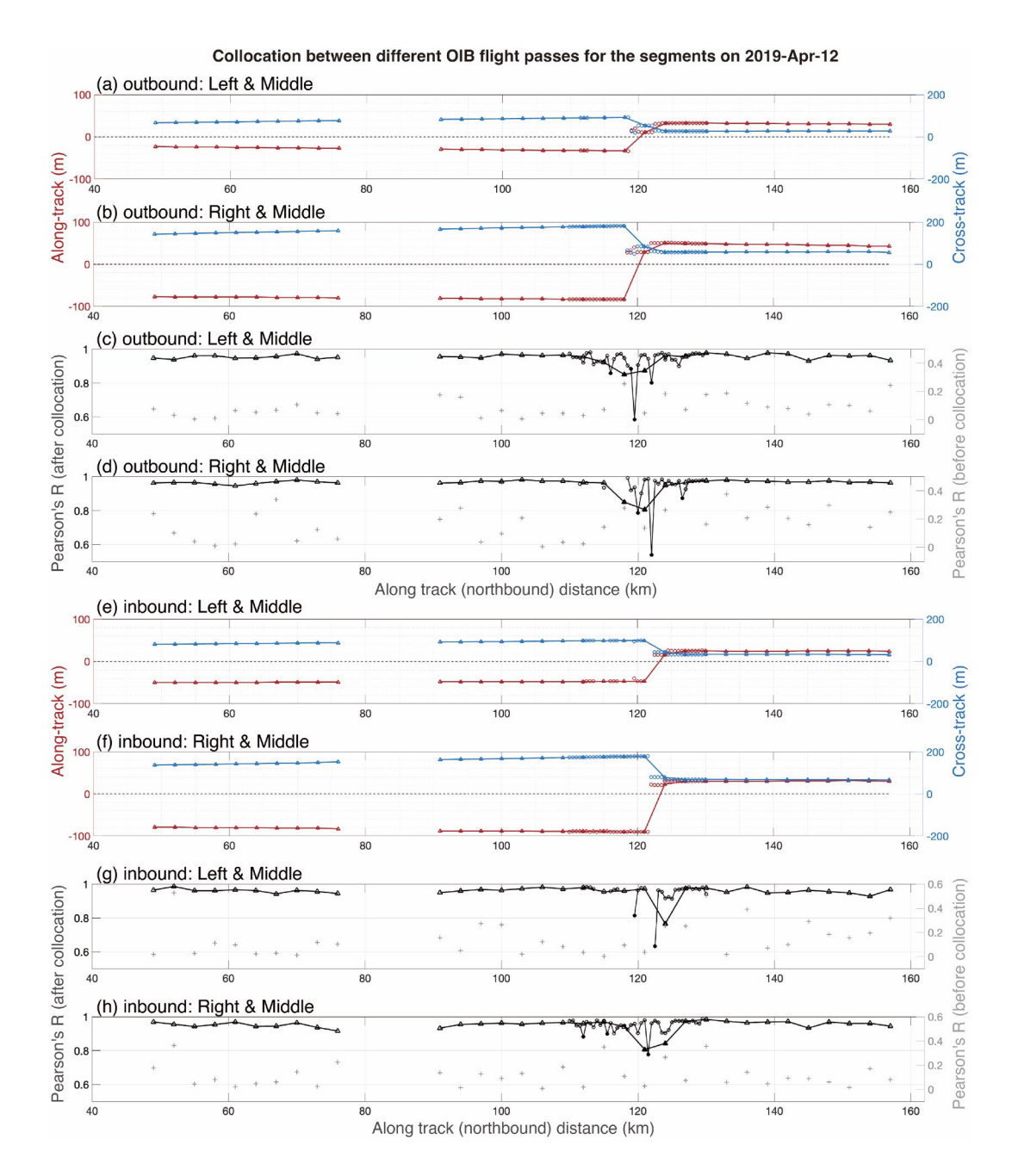


Figure A2. Same as Fig. A1, but for the OIB campaign on April 12th, 2019. Correlation coefficients lower than 0.8 are marked by filled symbols in panel c, d, g and h. For segments around the apparent deformation (at $\sim 120^{REVI:}$ km along the track), the local drift correction is further refined to $500^{REVI:}$ m in the along-track direction. The $500^{REVI:}$ m-scale drift corrections and the correlation coefficients are marked by circles and thin lines.

Table B1. REV2: OIB campaign and the corresponding S1 images. The corresponding ICESat2 ground tracks' information, including its visit times are shown in the last column.

OIB ATM	2019-Apr-08:	2019-Apr-12:
data	12:24:18 to 15:51:59	13:11:18 to 15:49:17
IS2 RGT	2019-Apr-08:	2019-Apr-12:
	RGT 0157	RGT 0218
	Beam 1,2,3,4	Beam 1,2,3,4
	13:09:59 to 13:10:39	13:03:21 to 13:03:54
S-1 Images	2019-Apr-07: S1B_EW_GRDM_1SDH_20190407T150052_20190407T150152_015702_01D768_1E98 2019-Apr-07: S1B_EW_GRDM_1SDH_20190407T145952_20190407T150052_015702_01D768_0AEC	
	2019-Apr-08: S1B_EW_GRDM_1SDH_20190408T140254_20190408T140354_015716_01D7D4_334A 2019-Apr-09:	
	S1B_EW_GRDM_1SDH_20190409T144345_20190409T144445_015731_01D856_468A 2019-Apr-01:	
	S1B_EW_GRDM_1SDH_20190401T141105_20190401T141205_015614_01D465_4CC6 2019-Apr-15:	
	S1A_EW_GRDM_1SDH_20190415T144457	_201904151144602_026802_030317_2C1F
	2019-Apr-12: S1B_EW_GRDM_1SDH_20190412T182436_20190412T182536_015777_01D9D0_7AB9 2019-Apr-11:	
	S1B_EW_GRDM_1SDH_20190411T174333_20190411T174433_015762_01D955_0683 2019-Apr-13:	
	S1B_EW_GRDM_1SDH_20190413T190536_20190413T190636_015792_01DA51_7539 2019-Apr-05:	
	S1B_EW_GRDM_1SDH_20190405T201050_20190405T201154_015676_01D68A_61C3 2019-Apr-19:	
	S1B_EW_GRDM_1SDH_20190419T195430	_20190419T195534_015880_01DD4B_40E2

Table B1 lists all the S1 EW images used in this study, specifically collected during the OIB campaigns on April 8th and 12th. Two types of images are included: those on the adjacent days of the campaigns, and those separated by about 1 week from the campaigns. The corresponding IS2 reference ground tracks (RGT) are also shown.

Appendix C: REVI: Statistical relationship between F_s and σ_0^{HV} for the segments on April 8th and 12th

For the two pairs of sample segments on April 8th and April 12th, the statistical relationship between F_s and the C-band backscatter in the HV-channel are shown below in Figure C1 and C2. Our results show general consistency with previous studies (Macdonald et al., 2024; Kortum et al., 2024), that freeboard generally correlates slightly better with the HV-channel than with the HH-channel backscatter. The statistical relationship between freeboard and backscatter in the HV-channel for all the OIB segments are also analyzed in this section (see Fig. C3).

The HV-channel backscatter is generally much weaker than the HH-channel. This is particularly evident for FYI, where HV backscatter often falls below the nominal noise floor (Segal et al., 2020). Additionally, the sub-swath artifacts are more evident in the HV-channel (i.e., abrupt transition of σ_0 across the sub-swath boundaries) for Sentinel-1 EW mode images (Lohse et al., 2021). Despite the stronger correlation observed in the HV band, the qualitative statistical relationship between freeboard and backscatter is similar when using either the HH or HV channel. Given these consideration, this work primarily concentrates on the S1 HH-channel.

The 9km sample segments on 2019-Apr-8

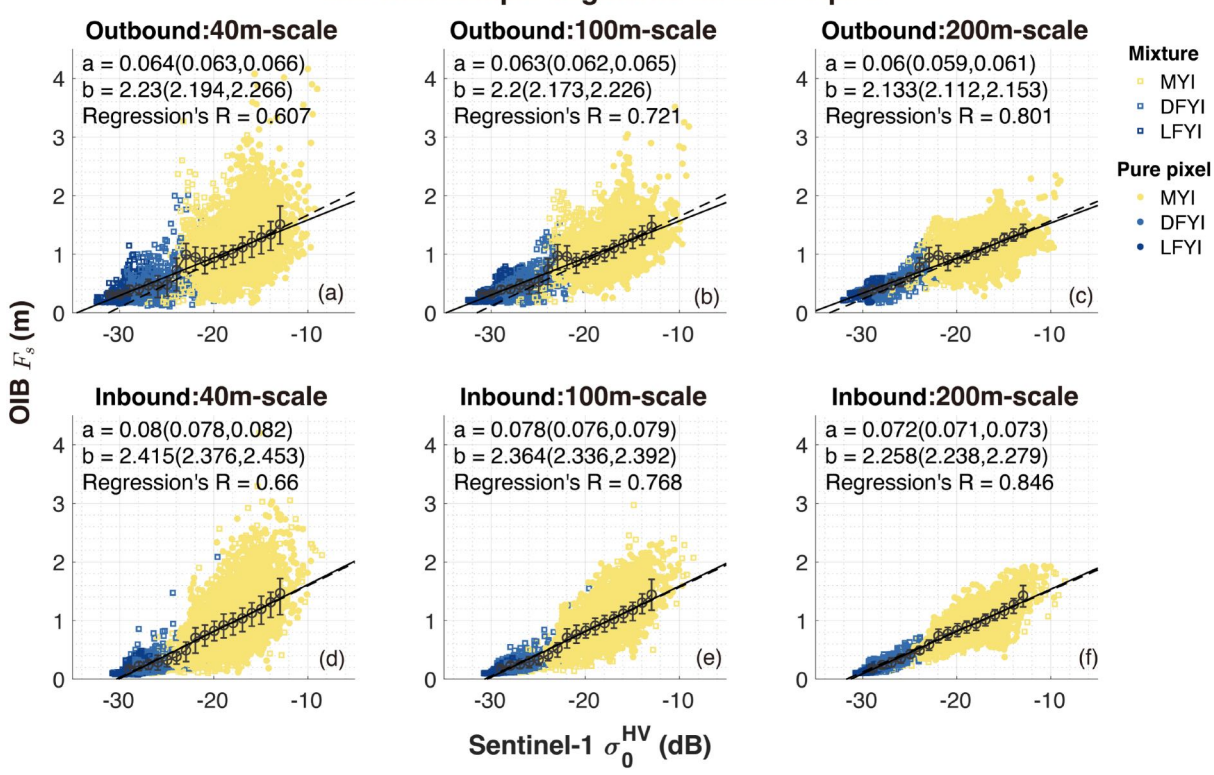


Figure C1. Scattered plot of the relationship between F_s and the Sentinel-1 C-band backscatter (σ_0) in the HV polarization channel for the sample segment Sequence of April 8th, 2019. Same as in Fig. 2, three spatial scales of F_s are adopted for matching to the 40m-resolution σ_0 product: 40m (left column), 100m (middle column) and 200m (right column).

Author contributions. SX carried out conceptualization of the study. SL processed the OIB dataset. WG processed S1 images and provided sea ice type maps. SL, WG, YF, SX carried out the analysis, with input from other authors. All author contributed to the writing of the manuscript.

Competing interests. The authors declare that they have no competing interests.

Acknowledgements. This work is mainly supported by the joint project of INTERAAC, co-funded by the National Key R&D Program of China (grant no.: 2022YFE0106700) and the Research Council of Norway (grant no.: 328957). JCL is partially supported by the SUDARCO (Forskning for god forvaltning av Polhavet) project under the Fram Centre (#2551323), the DynAMIC (Detecting episodes of Arctic sea ice Mass Imbalance) project under RCN (#343069), and the SI/3D (Summer Sea Ice in 3D) project under the European Research Council,

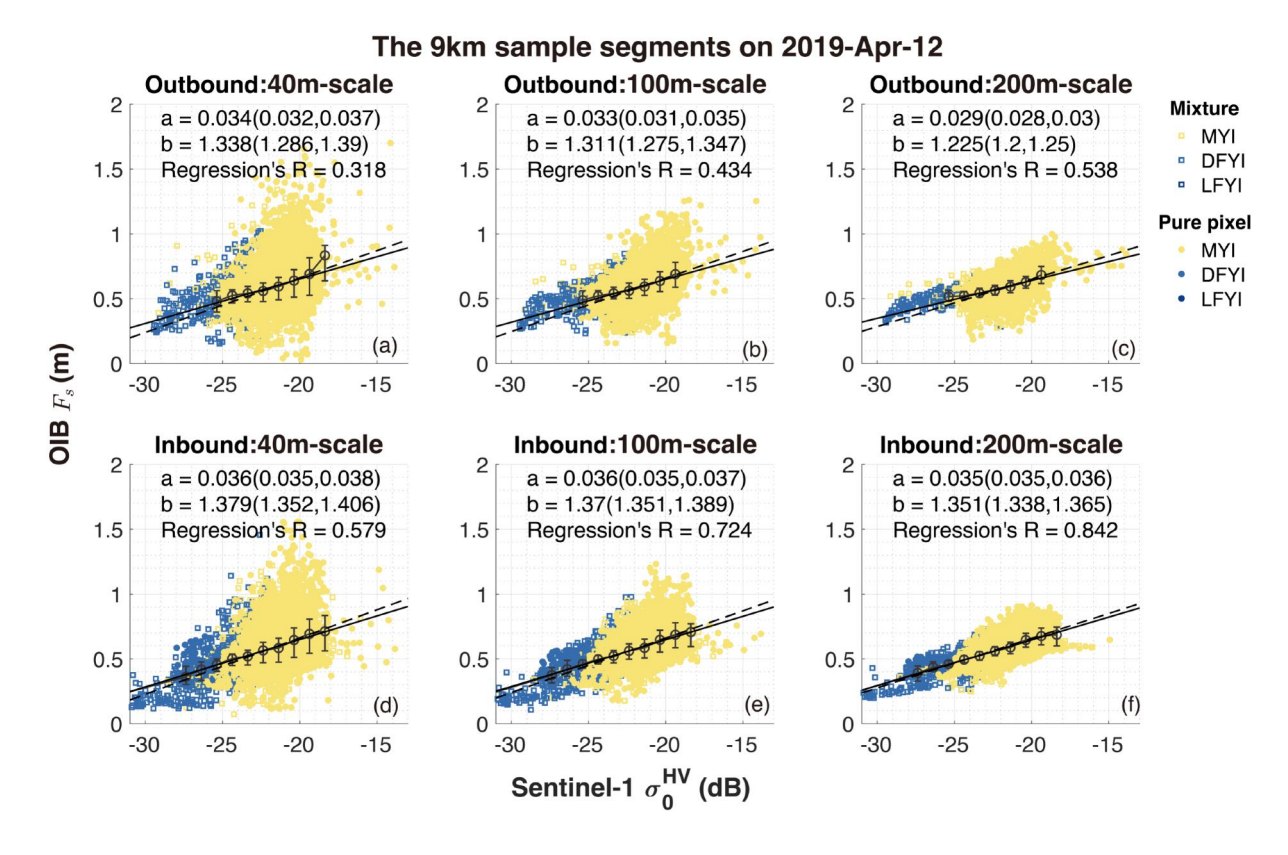


Figure C2. Same as Fig. C1, but for the sample segment^{REVI}:s on April 12th, 2019.

ERC (#101077496). SX is also partially supported by the National Natural Science Foundation of China (grant no.: 42030602) and the International Partnership Program of Chinese Academy of Sciences (grant no.: 183311KYSB20200015).

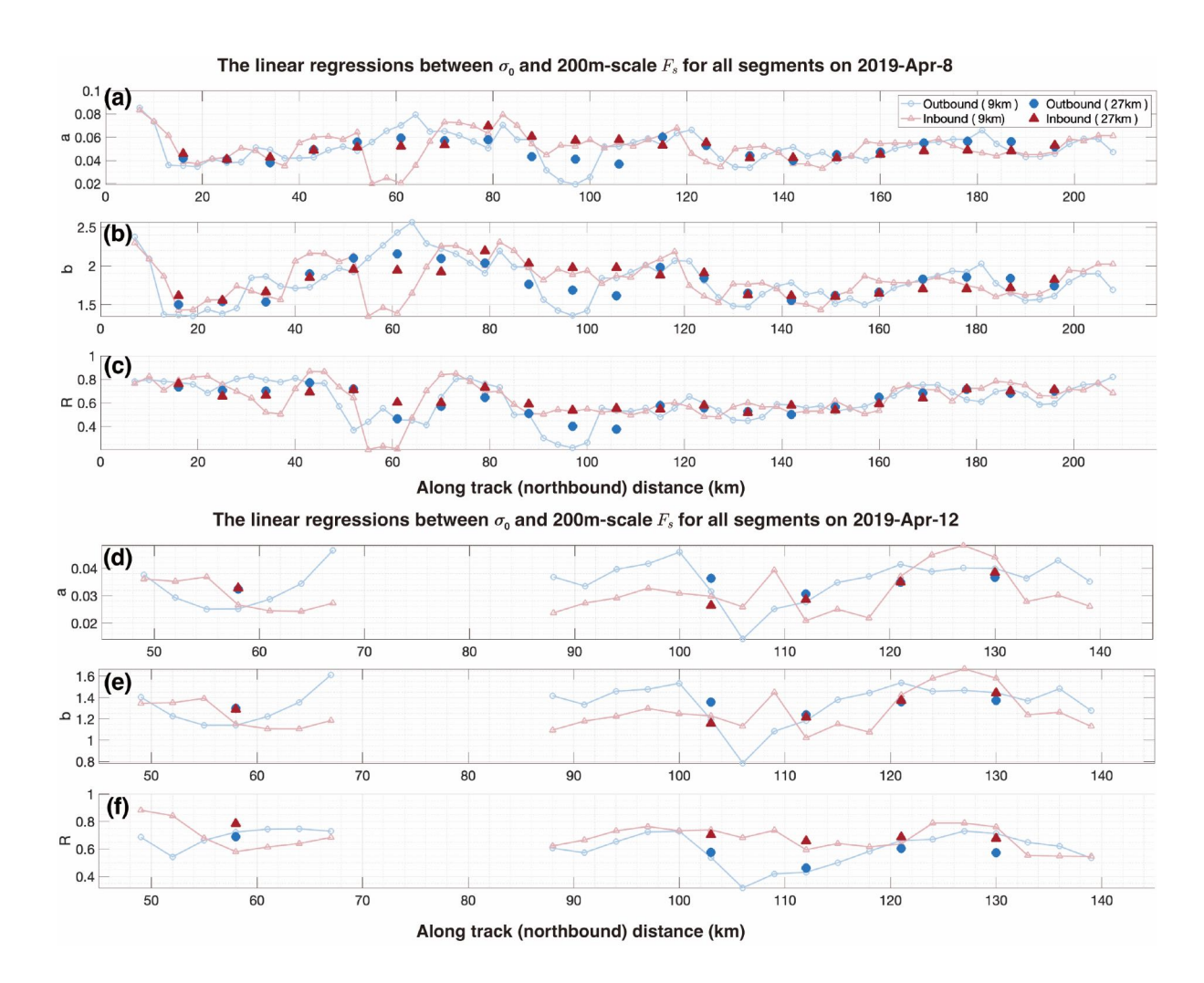


Figure C3. Same as Fig. 6, but for HV channel

590 References

De Zan, F. and Guarnieri, A. M.: TOPSAR: Terrain observation by progressive scans, IEEE Transactions on Geoscience and Remote Sensing, 44, 2352–2360, 2006.

Doulgeris, A. P.: An automatic U-distribution and markov random field segmentation algorithm for PolSAR images, IEEE Transactions on Geoscience and Remote Sensing, 53, 1819–1827, https://doi.org/10.1109/TGRS.2014.2349575, 2015.

595 Duncan, K. and Farrell, S. L.: Determining Variability in Arctic Sea Ice Pressure Ridge Topography With ICESat-2, Geophysical Research Letters, 49, e2022GL100272, https://doi.org/10.1029/2022GL100272, e2022GL100272 2022GL100272, 2022.

Farrell, S. L., Laxon, S. W., McAdoo, D. C., Yi, D., and Zwally, H. J.: Five years of Arctic sea ice freeboard measurements from the Ice, Cloud and land Elevation Satellite, Journal of Geophysical Research: Oceans, 114, https://doi.org/10.1029/2008JC005074, 2009.

- Geldsetzer, T. and Howell, S. E.: Incidence angle dependencies for C-band backscatter from sea ice during both the winter and melt season,

 IEEE Transactions on Geoscience and Remote Sensing, 61, 1–15, 2023.
 - Guo, W., Itkin, P., Lohse, J., Johansson, M., and Doulgeris, A. P.: Cross-platform classification of level and deformed sea ice considering per-class incident angle dependency of backscatter intensity, The Cryosphere, 16, 237–257, https://doi.org/10.5194/tc-16-237-2022, 2022.
 - Guo, W., Landy, J., Lohse, J., Doulgeris, A. P., Johansson, M., Eltoft, T., Itkin, P., and Xu, S.: Towards a multi-decadal SAR analysis of sea ice types in the Atlantic sector of the Arctic Ocean, IEEE Journal of Selected Topics in Applied Earth Observations and Remote Sensing, 2025.

605

625

- Kankaku, Y., Suzuki, S., and Osawa, Y.: ALOS-2 mission and development status, in: 2013 IEEE International Geoscience and Remote Sensing Symposium-IGARSS, pp. 2396–2399, IEEE, 2013.
- Kim, Y.-S., Onstott, R., and Moore, R.: Effect of a snow cover on microwave backscatter from sea ice, IEEE Journal of Oceanic engineering, 9, 383–388, 1984.
- Kortum, K., Singha, S., and Spreen, G.: Sea Ice Freeboard Extrapolation from ICESat-2 to Sentinel-1, EGUsphere, 2024, 1–16, https://doi.org/10.5194/egusphere-2024-3351, 2024.
 - Krumpen, T., von Albedyll, L., Bünger, H. J., Castellani, G., Hartmann, J., Helm, V., Hendricks, S., Hutter, N., Landy, J. C., Lisovski, S., Lüpkes, C., Rohde, J., Suhrhoff, M., and Haas, C.: Smoother sea ice with fewer pressure ridges in a more dynamic Arctic, Nature Climate Change, 15, 66–72, https://doi.org/10.1038/s41558-024-02199-5, 2025.
- Kwok, R.: Arctic sea ice thickness, volume, and multiyear ice coverage: losses and coupled variability (1958–2018), Environmental Research Letters, 13, 105 005, https://doi.org/10.1088/1748-9326/aae3ec, 2018.
 - Kwok, R., Kacimi, S., Markus, T., Kurtz, N. T., Studinger, M., Sonntag, J. G., Manizade, S. S., Boisvert, L. N., and Harbeck, J. P.: ICESat-2 Surface Height and Sea Ice Freeboard Assessed with ATM Lidar Acquisitions from Operation IceBridge, Geophysical Research Letters, 46, 11 228–11 236, https://doi.org/10.1029/2019GL084976, 2019.
- Lavergne, T. and Down, E.: A climate data record of year-round global sea-ice drift from the EUMETSAT Ocean and Sea Ice Satellite Application Facility (OSI SAF), Earth System Science Data, 15, 5807–5834, https://doi.org/10.5194/essd-15-5807-2023, 2023.
 - Livingstone, C. E. and Drinkwater, M. R.: Springtime C-band SAR backscatter signatures of Labrador Sea marginal ice: measurements versus modeling predictions, IEEE Transactions on Geoscience and Remote Sensing, 29, 29–41, 1991.
 - Lohse, J., Doulgeris, A. P., and Dierking, W.: Mapping sea-ice types from Sentinel-1 considering the surface-type dependent effect of incidence angle, Annals of Glaciology, 61, 260–270, https://doi.org/10.1017/aog.2020.45, 2020.
 - Lohse, J., Doulgeris, A. P., and Dierking, W.: Incident Angle Dependence of Sentinel-1 Texture Features for Sea Ice Classification, Remote Sensing, 13, https://doi.org/10.3390/rs13040552, 2021.
 - Macdonald, G. J., Scharien, R. K., Duncan, K., Farrell, S. L., Rezania, P., and Tavri, A.: Arctic Sea Ice Topography Information From RADARSAT Constellation Mission (RCM) Synthetic Aperture Radar (SAR) Backscatter, Geophysical Research Letters, 51, e2023GL107261, https://doi.org/10.1029/2023GL107261, e2023GL107261 2023GL107261, 2024.
 - MacGregor, J. A., Boisvert, L. N., Medley, B., Petty, A. A., Harbeck, J. P., Bell, R. E., Blair, J. B., Blanchard-Wrigglesworth, E., Buckley, E. M., Christoffersen, M. S., Cochran, J. R., Csatha, B. M., De Marco, E. L., Dominguez, R. T., Fahnestock, M. A., Farrell, S. L., Gogineni, S. P., Greenbaum, J. S., Hansen, C. M., Hofton, M. A., Holt, J. W., Jezek, K. C., Koenig, L. S., Kurtz, N. T., Kwok, R., Larsen, C. F., Leuschen, C. J., Locke, C. D., Manizade, S. S., Martin, S., Neumann, T. A., Nowicki, S. M., Paden, J. D., Richter-Menge, J. A.,
- Rignot, E. J., Rodriguez-Morales, F., Siegfried, M. R., Smith, B. E., Sonntag, J. G., Studinger, M., Tinto, K. J., Truffer, M., Wagner,

- T. P., Woods, J. E., Young, D. A., and Yungel, J. K.: The Scientific Legacy of NASA's Operation IceBridge, Reviews of Geophysics, 59, e2020RG000712, https://doi.org/10.1029/2020RG000712, 2021.
- Makynen, M., Manninen, A. T., Simila, M., Karvonen, J. A., and Hallikainen, M. T.: Incidence angle dependence of the statistical properties of C-band HH-polarization backscattering signatures of the Baltic Sea ice, IEEE Transactions on Geoscience and Remote Sensing, 40, 2593–2605, 2003.

640

- Manninen, A.: Effects of ice ridge properties on calculated surface backscattering in BEPERS-88, International Journal of Remote Sensing, 13, 2469–2487, 1992.
- Mansourpour, M., Rajabi, M., and Blais, J.: Effects and performance of speckle noise reduction filters on active radar and SAR images, in: Proc. Isprs, vol. 36, p. W41, 2006.
- Markus, T., Neumann, T., Martino, A., Abdalati, W., Brunt, K., Csatho, B., Farrell, S., Fricker, H., Gardner, A., Harding, D., Jasinski, M., Kwok, R., Magruder, L., Lubin, D., Luthcke, S., Morison, J., Nelson, R., Neuenschwander, A., Palm, S., Popescu, S., Shum, C., Schutz, B. E., Smith, B., Yang, Y., and Zwally, J.: The Ice, Cloud, and land Elevation Satellite-2 (ICESat-2): Science requirements, concept, and implementation, Remote Sensing of Environment, 190, 260–273, https://doi.org/10.1016/j.rse.2016.12.029, 2017.
- Marsan, D., Stern, H., Lindsay, R., and Weiss, J.: Scale Dependence and Localization of the Deformation of Arctic Sea Ice, Phys. Rev. Lett., 93, 178 501, https://doi.org/10.1103/PhysRevLett.93.178501, 2004.
 - MDA: RADARSAT CONSTELLATION MISSION PRODUCT SPECIFICATION, Tech. Rep. RCM-SP-52-9092, Canadian Space Agency, 2021.
 - Miranda, N., Rosich, B., Meadows, P. J., Haria, K., Small, D., Schubert, A., Lavalle, M., Collard, F., Johnsen, H., Guarnieri, A. M., and D'Aria, D.: The EnviSAT ASAR Mission: A Look Back At 10 Years Of Operation, in: ESA Living Planet Symposium, vol. 722 of *ESA Special Publication*, p. 41, 2013.
 - Neumann, T., Brunt, K., Marguder, L., and Kurtz, N.: Validation activities for the ice, cloud, and land elevation satellite-2 (ICESat-2) mission, in: EGU General Assembly Conference Abstracts, p. 20671, 2020.
 - Nicolaus, M., Perovich, D. K., Spreen, G., Granskog, M. A., von Albedyll, L., Angelopoulos, M., Anhaus, P., Arndt, S., Belter, H. J., Bessonov, V., Birnbaum, G., Brauchle, J., Calmer, R., Cardellach, E., Cheng, B., Clemens-Sewall, D., Dadic, R., Damm, E., de Boer,
- G., Demir, O., Dethloff, K., Divine, D. V., Fong, A. A., Fons, S., Frey, M. M., Fuchs, N., Gabarró, C., Gerland, S., Goessling, H. F., Gradinger, R., Haapala, J., Haas, C., Hamilton, J., Hannula, H.-R., Hendricks, S., Herber, A., Heuzé, C., Hoppmann, M., HÞyland, K. V., Huntemann, M., Hutchings, J. K., Hwang, B., Itkin, P., Jacobi, H.-W., Jaggi, M., Jutila, A., Kaleschke, L., Katlein, C., Kolabutin, N., Krampe, D., Kristensen, S. S., Krumpen, T., Kurtz, N., Lampert, A., Lange, B. A., Lei, R., Light, B., Linhardt, F., Liston, G. E., Loose, B., Macfarlane, A. R., Mahmud, M., Matero, I. O., Maus, S., Morgenstern, A., Naderpour, R., Nandan, V., Niubom, A., Oggier,
- M., Oppelt, N., Patzold, F., Perron, C., Petrovsky, T., Pirazzini, R., Polashenski, C., Rabe, B., Raphael, I. A., Regnery, J., Rex, M., Ricker, R., Riemann-Campe, K., Rinke, A., Rohde, J., Salganik, E., Scharien, R. K., Schiller, M., Schneebeli, M., Semmling, M., Shimanchuk, E., Shupe, M. D., Smith, M. M., Smolyanitsky, V., Sokolov, V., Stanton, T., Stroeve, J., Thielke, L., Timofeeva, A., Tonboe, R. T., Tavri, A., Tsamados, M., Wagner, D. N., Watkins, D., Webster, M., and Wendisch, M.: Overview of the MOSAiC expedition: Snow and sea ice, Elementa: Science of the Anthropocene, 10, 000 046, https://doi.org/10.1525/elementa.2021.000046, 2022.
- Ning, C., Xu, S., Zhang, Y., Wang, X., Fan, Z., and Liu, J.: Lagrangian tracking of sea ice in Community Ice CodE (CICE; version 5), Geoscientific Model Development, 17, 6847–6866, https://doi.org/10.5194/gmd-17-6847-2024, 2024.
 - Onstott, R. G.: SAR and Scatterometer Signatures of Sea Ice, chap. 5, pp. 73–104, American Geophysical Union (AGU), https://doi.org/10.1029/GM068p0073, 1992.

- Petty, A. A., Tsamados, M. C., Kurtz, N. T., Farrell, S. L., Newman, T., Harbeck, J. P., Feltham, D. L., and Richter-Menge, J. A.: Characterizing Arctic sea ice topography using high-resolution IceBridge data, The Cryosphere, 10, 1161–1179, 2016.
 - Petty, A. A., Tsamados, M. C., and Kurtz, N. T.: Atmospheric form drag coefficients over Arctic sea ice using remotely sensed ice topography data, spring 2009–2015, Journal of Geophysical Research: Earth Surface, 122, 1472–1490, https://doi.org/10.1002/2017JF004209, 2017.
 - Rampal, P., Weiss, J., Marsan, D., Lindsay, R., and Stern, H.: Scaling properties of sea ice deformation from buoy dispersion analysis, Journal of Geophysical Research: Oceans, 113, https://doi.org/10.1029/2007JC004143, 2008.
- Ricker, R., Fons, S., Jutila, A., Hutter, N., Duncan, K., Farrell, S. L., Kurtz, N. T., and Fredensborg Hansen, R. M.: Linking scales of sea ice surface topography: evaluation of ICESat-2 measurements with coincident helicopter laser scanning during MOSAiC, The Cryosphere, 17, 1411–1429, https://doi.org/10.5194/tc-17-1411-2023, 2023.
 - Segal, R. A., Scharien, R. K., Cafarella, S., and Tedstone, A.: Characterizing winter landfast sea-ice surface roughness in the Canadian Arctic Archipelago using Sentinel-1 synthetic aperture radar and the Multi-angle Imaging SpectroRadiometer, Annals of Glaciology, 61, 284–298, 2020.

- Shimada, M., Tadono, T., and Rosenqvist, A.: Advanced Land Observing Satellite (ALOS) and monitoring global environmental change, Proceedings of the IEEE, 98, 780–799, 2009.
- Sumata, H., de Steur, L., Divine, D. V., Granskog, M. A., and Gerland, S.: Regime shift in Arctic Ocean sea ice thickness, Nature, 615, 443–449, https://doi.org/10.1038/s41586-022-05686-x, 2023.
- 690 Sun, Y. and Li, X.-M.: Denoising Sentinel-1 Extra-Wide Mode Cross-Polarization Images Over Sea Ice., IEEE Trans. Geosci. Remote. Sens., 59, 2116–2131, 2021.
 - Tsai, Y.-L. S., Dietz, A., Oppelt, N., and Kuenzer, C.: Remote sensing of snow cover using spaceborne SAR: A review, Remote Sensing, 11, 1456, 2019.
- Xu, S., Zhou, L., Liu, J., Lu, H., and Wang, B.: Data Synergy between Altimetry and L-Band Passive Microwave Remote Sensing for the Retrieval of Sea Ice Parameters—A Theoretical Study of Methodology, Remote Sensing, 9, 1079, https://doi.org/10.3390/rs9101079, 2017.
 - Xu, S., Zhou, L., and Wang, B.: Variability scaling and consistency in airborne and satellite altimetry measurements of Arctic sea ice, The Cryosphere, 14, 751–767, https://doi.org/10.5194/tc-14-751-2020, 2020.